MEASUREMENT OF VIGILANCE USING EEG SOURCE LOCALIZATION

by

Salma Khaled Mohamad Zeid

A Thesis presented to the Faculty of the
American University of Sharjah
College of Engineering
In Partial Fulfillment
of the Requirements
for the Degree of

Master of Science in
Electrical Engineering

Sharjah, United Arab Emirates

November 2017

Approval Signatures

We, the undersigned, approve the Master's Thesis of Salma Khaled Mohamad Zeid.

Thesis Title: Measurement of Vigilance Using EEG Source Localization.

Signature	**Date of Signature** (dd/mm/yyyy)
_____	_____
Dr. Hasan Al-Nashash Professor, Department of Electrical Engineering Thesis Advisor	
_____	_____
Dr. Hasan Mir Associate Professor, Department of Electrical Engineering Thesis Co-Advisor	
_____	_____
Dr. Nasser Qaddoumi Professor, Department of Electrical Engineering Thesis Committee Member	
_____	_____
Dr. Salam Dhou Assistant Professor, Department of Computer Engineering Thesis Committee Member	
_____	_____
Dr. Nasser Qaddoumi Head, Department of Electrical Engineering	
_____	_____
Dr. Ghaleb Husseini Associate Dean for Graduate Affairs and Research College of Engineering	
_____	_____
Dr. Richard Schoephoerster Dean, College of Engineering	
_____	_____
Dr. Mohamed El-Tarhuni Vice Provost for Graduate Studies	

Acknowledgement

First of all I would like to thank the American University of Sharjah for supporting me throughout my bachelor's and master's study journey. I am immeasurably grateful to AUS for providing me with a Graduate Teaching Assistantship, without which I would not have been able to pursue my master's degree. I want to immensely thank my advisors Dr. Hasan Al-Nashash and Dr. Hasan Mir for their limitless guidance and continuous support throughout my thesis journey. Without their patience and constructive criticism, after Allah's reconcilement, none of this work would have been possible.

I would like to thank my whole family for believing in me when I doubted what I can achieve. The endless calls from my grandparents and siblings checking up on me and their motivational talks are what kept me going. I am grateful to my husband who was always next to me in the good and the bad. Finally, those who can never be repaid, my loving parents who have been my pillar of strength; without whom I wouldn't believe that "these mountains you are carrying, you were only supposed to climb" – Najwa Zebian.

Allah has made it all possible…

Abstract

Vigilance, or sustained attention, is crucial for jobs where attentiveness for prolonged times is required. These jobs include air traffic control, luggage inspection, and surveillance jobs. Vigilance decrement can cause catastrophic consequences. Therefore, vigilance level assessment is a widely-researched topic. Several methods have been used to assess vigilance levels such as eye tracking techniques which include monitoring saccadic eye movements and pupil size variation. Other methods used are heart rate variability, and physiological data such as electrocardiogram (ECG), electro-oculogram (EoG) and electroencephalogram (EEG). EEG data has been found to have strong correlations with human's vigilance level. This thesis report presents a novel method for the assessment of vigilance decrement using EEG data that embarks upon the brain's temporal behavior. An experiment based on a 20 to 30-minute Psychomotor Vigilance Task (PVT), that simulates real applications where vigilance decrement is observed, was carried out on 33 subjects and their EEG recordings and reaction times were collected. In the PVT task, subjects were required to respond to target events while refraining from non-target events. Vigilance reinforcement by challenge integration was tested where 22 out of the 33 subjects had an additional task where they had to respond to noisy target events. The spectral power density characteristics namely the delta, theta, alpha and beta waves of the EEG data are compared for low and high vigilance states. Furthermore, EEG source localization is utilized to monitor source dynamics of the brain in transition from vigilance states. Results from both methods are analyzed using Student's t-test with the significance threshold set at 0.1. Power spectral density analysis showed that power in *AF8* electrode in delta, theta and alpha bands increased with vigilance decrement with p-values .023, .079 and .020 respectively. The source localization approach showed an increase in prefrontal source distribution with vigilance decrement with p-value of .015. The joint probability function of the prefrontal delta, theta and alpha bands as well as the source dynamics of prefrontal activity showed promise in constructing a vigilance assessment model to identify vigilance state from labeled data by yielding an 84.85% accurate detection.

Keywords: ***Vigilance decrement; electroencephalogram; brainwaves; power spectral density; source localization.***

Table of Contents

List of Figures

List of Tables

Chapter 1: Introduction

1.1 Vigilance Decrement Assessment

Vigilance is a term with various definitions but is mostly used as sustained attention or tonic alertness. Vigilance implies the degree of cognitive performance. Many interacting neural systems affect vigilance [1]. Researchers have found that people who participated in sustained attention type tasks suffered a noticeable decrease in their ability to detect critical stimuli over time. This phenomenon is known as vigilance decrement. The vigilance decrement can be characterized either by a decrease in target stimuli detection or an increase in the reaction time to that stimulus.

There are two opposing theories of vigilance decrement: the mindlessness theory and the resource depletion theory [2]. The *mindlessness*, or *boredom*, theory suggests that the person monitoring loses focus of attention due to the long intervals separating infrequent critical signals, where they start treating their vigilance assignment in a spontaneous automatic manner [2]. The lack of external support for attention during the intervals between critical signals fails to keep observers attentive to the task which leads to their loss of ability to properly detect target stimuli. This is also known as the *under-load* hypothesis [3]. Whereas the *resource depletion*, also known as *mental fatigue* or *over-load*, theory attributes vigilance decrement to the insufficient available cognitive resources as observers are required to make continuous discrimination between target stimuli among other noise signals under conditions of uncertainty. This continuous demand on information processing resources does not allow for replenishment of those resources which causes the decline of vigilance over time [3].

Many tasks such as air traffic control, luggage screening in airports, driving and surveillance occupations require high vigilance levels. However, due to their monotonous nature, the personnel performing the task suffer from vigilance decrement, which can lead to disastrous penalties. This vigilance decrement due to monotony of tasks resembles the mindlessness theory. Therefore, this report adapts the under-load hypothesis by investigating methods that can measure the vigilance level in monotonous tasks. Various methods in assessing vigilance decrement have been proposed in the literature. Ranging from eye tracking techniques, to heart rate dynamics, and physiological tests have been used to detect changes in vigilance

levels. Predominately, electroencephalogram (EEG) data has been used to evaluate vigilance by investigating the power spectral density changes with vigilance in brain waves, namely: delta, theta, alpha and beta waves. In chapter 3, a detailed literature review of the various methods used for the assessment of vigilance decrement will be presented. In this thesis work, we aim to use a novel method for the assessment of vigilance using brain source localization.

1.2 Brain Source Localization

EEG signals are an example of physiological data that has been tightly correlated to vigilance. EEG is a noninvasive functional neuroimaging technique that measures scalp potentials due to firing of neurons (brain cells) in response to different stimuli. EEG is useful in analysis of spatial and temporal activities in the brain. Despite its low spatial resolution, EEG has high temporal resolution of about a few milliseconds which makes it appropriate for real-time monitoring of brain activity [4]. As mentioned earlier, the most studied characteristic of EEG signals in accordance with alertness level is power spectral density of different brain waves. Additionally, EEG signals are used to analyze event related potentials (ERPs) which aids in studying brain activity with respect to certain evoked stimuli.

To study the spatial aspect of brain activity, EEG source localization has been developed. In EEG source localization, first the *forward problem* is solved where volume conductor head models are used to obtain electric fields outside the scalp given specific neural activity. A mathematical representation of the forward problem is formulated where neurons producing the electric signals are modeled as current dipoles. However, given the electric potentials on the scalp, the source of brain activity cannot be uniquely calculated as many source configurations can produce the same EEG pattern. Therefore, a-priori assumptions on the production of EEG signals are made to solve the *inverse problem*. In order to solve the inverse problem, which involves localizing the source of neural activity, various techniques such as array processing and Bayesian methods are implemented for accurate localization. Discussion of different source localization methods are presented in chapter 4.

1.3 Motivation and problem statement

Vigilance decrement can cause fatalities in several critical tasks such as monotonous driving, surveillance, and airport security. Early detection of this decrement can allow taking control of the situation before any appalling costs. Therefore, the prime objective of this work is the construction of a vigilance measurement model using EEG source localization. The main challenge in this effort is developing an accurate vigilance measuring system that can detect vigilance decrement in critical conditions by monitoring different neural sources and their corresponding current densities in real-time ensuring high temporal and spatial resolutions.

1.4 Thesis Methodology and Outline

In this work, Advanced Source Analysis (ASA-lab) software is used to collect and analyze EEG data from 33 subjects while performing a task that induces vigilance decrement under controlled conditions. The task involves the subject reacting to target events among other non-target events. The recorded raw EEG data is a waveform that not only contains brain activity, but also comprises of other random unwanted signals called artefacts such as eye blinks, eye movements, muscle movements, electromyography (EMG), and electrocardiogram (ECG). Consequently, the EEG signals are preprocessed to remove unwanted signals to get a clean EEG signal showing only the subject's brain activity. Furthermore, the signal is filtered to keep only frequency components of interest which is typically 0.5-30 Hz. The spectral behavior of the EEG data is investigated and compared between low and high vigilance states. Moreover, source localization SAFFIRE algorithm, is used to examine the changing aspects of the sources from low and high vigilance states. Both results are used to produce a model for assessment of vigilance level. The rest of the report is organized as follows: chapter 2 presents the brain anatomy. EEG and other brain imaging techniques are also discussed and compared. Chapter 3 summaries previous works on vigilance decrement assessment. In chapter 4 source localization is introduced and the mathematical modelling of the forward and inverse problems is outlined along with the description of different source localization algorithms. The experimental setup is explained in chapter 5. Data preprocessing and results are presented in chapter 6. Finally, chapter 7 includes discussion, conclusions and future work.

Chapter 2: Brain Anatomy

2.1 Brain Structure

The brain is a complex multilayered organ divided into a hierarchical structure (Figure 1): the brainstem, the cerebellum, the thalamus, and the cerebrum. The brainstem is located at the bottom of the brain connecting it to the spinal cord which branches throughout the body through neural networks. It is responsible for basic functions such as breathing, circulation, digestion, and other basic involuntary functions. It routes and filters the sensory information up to the brain and the motor responses back to the body through the spinal cord. The cerebellum is located at the lower rear of the brain where it houses motor control and motion memory. The thalamus, above the brainstem, acts as a router which sorts the sensory data and sends it across the brain where it needs to go. Below the thalamus, there is the hypothalamus which is responsible for homeostasis. The cerebrum is the most dominant and the largest part of the brain, occupying more than three quarters of the brain's total volume [5]. It comprises the major brain division known as the forebrain where high order information processing and perception takes place. The cerebrum is divided into hemispheres: the left hemisphere and the right hemisphere which are linked through a bridge of nerve fibers called the corpus callosum.

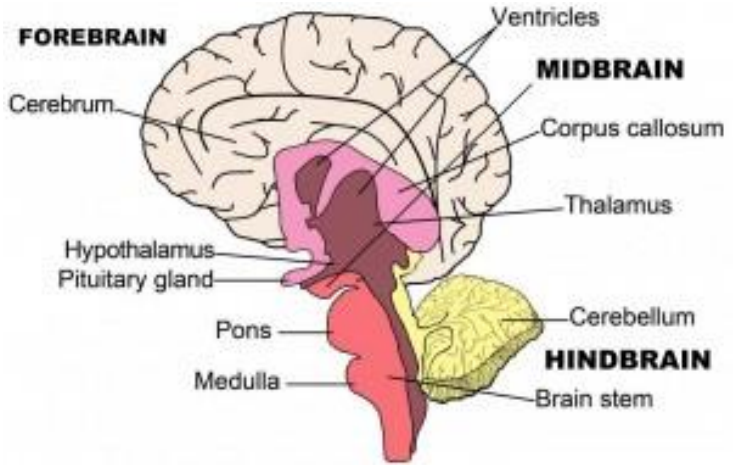

Figure 1: Brain Structure (Source: http://nbia.ca/brain-structure-function/)

2.1.1 Cerebral Cortex. The cerebral cortex is the outer wrinkled layer of the cerebrum known as the grey matter where most of the high order processing occurs. Due to the wrinkled nature of the cortex and its thickness of 2 to 5 mm, it is made up of to 10 to 50 billion neurons, allowing different parts of the brain to communicate [5].

The cortex and is divided into four main lobes as shown in Figure 2: the frontal, parietal, temporal, and occipital lobes. Each of these lobes have different functions, where the frontal lobe is associated with reasoning, motor skills, higher level cognition, and expressive language. The parietal lobe is associated with processing tactile sensory information. The temporal lobe is important for speech perception and memory, while the occipital lobe is responsible for interpreting visual stimuli and information [6].

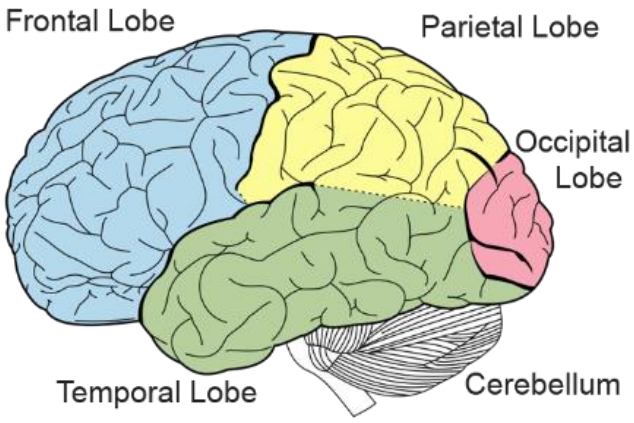

Figure 2: The cerebral cortex (Source: http://controlmind.info/human-brain/structure-of-the-brain)

Certain cortical regions have rather simpler functions, termed the primary cortices which are areas that directly receive sensory input such as: vision, hearing, somatic sensation, or that are directly involved in motor responses. The association cortices, however, serve more complex functions including memory, language, abstraction, creativity, judgment, emotion, and attention [6]. Regions of association cortex are adjacent to the primary cortices and include much of the rostral part of the frontal lobes, as well as regions encompassing areas of the posterior parietal lobe, the temporal lobe, and the anterior part of the occipital lobes [6].

2.1.2 Brain cells. The brain is made up of two types of cells: Neurons and glial cells. Neurons are cells that send and receive electro-chemical signals to and from other neurons across the brain and the body, while glial cells provide support functions for the neurons and are much more abundant.

2.1.2.1 Neurons. Neurons are nerve cells that transmit nerve signals to and from the brain. It consists of a soma or cell body with branching dendrites that act as signal

receivers from other neurons as seen in Figure 3. The axon is a projection extending from the cell body which conducts the nerve signal and transmits it through its terminals to a synapse, a gap between the axon terminal and the receiving cell, by means of chemical messengers called neurotransmitters. The axon is coated by a myelin sheet which allows for fast transmission of action potentials (discussed in section 2.2.1).

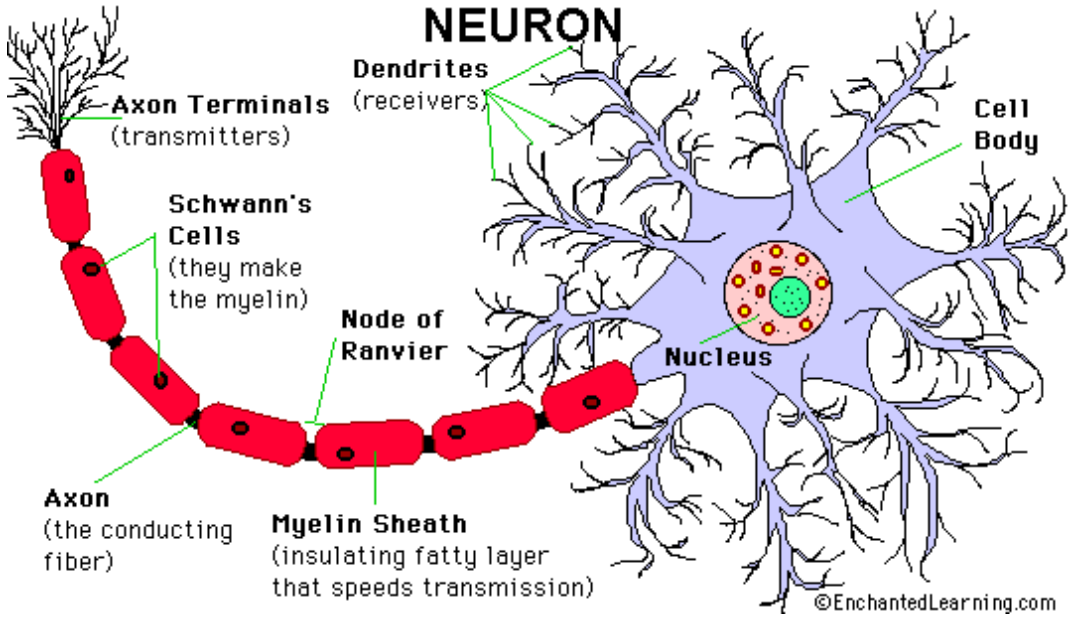

Figure 3: Neuron Structure (Source: http://www.enchantedlearning.com/subjects/anatomy/brain/Neuron.shtml)

2.2 Brain Electrical Activity

2.2.1 Nerve Impulses. The transmission of a nerve impulse along a neuron from one end to the other occurs due to the change in the electrical charge across its membrane. The membrane of an unstimulated neuron is naturally polarized. This is due to excess sodium ions (Na^+) on the outside of the membrane and an excess of potassium ions (K^+) on the inside which are continually leaking across the membrane through *leakage channels.* The resting or unstimulated membrane is more permeable to potassium ions than to sodium ions, while large negatively charged ions such as proteins and nucleic acids reside within the cell causing a resting potential of -70 millivolts inside the membrane with respect to the outside [8].

A graded potential is one that does not travel far from its origin and usually occurs in cell bodies and dendrites due to a stimulus such as light, heat or neurotransmitters that causes Na^+ *gated channels* to open making the membrane more

positive (depolarizes) or K^+ *gated channels* to open making the membrane more negative (hyperpolarizes). If a depolarizing graded potential is sufficiently large that it exceeds the threshold potential, an *action potential*, or a complete depolarization (from -70 mV to around +30 mV) is caused [8]. This stimulates neighboring Na^+ gates down the axon to open and thus traveling down the axon to other neurons. An action potential is an all or nothing event: if the threshold potential is exceeded, complete depolarization occurs. As a response, the K^+ channels open allowing the outflow of positive potassium ions making the membrane hyperpolarized. During refractory period the Na^+ and K^+ ions switch places through pumps in the cell membrane until returning to original resting potential (Figure 4). Unlike graded potential, an action potential can travel long distances.

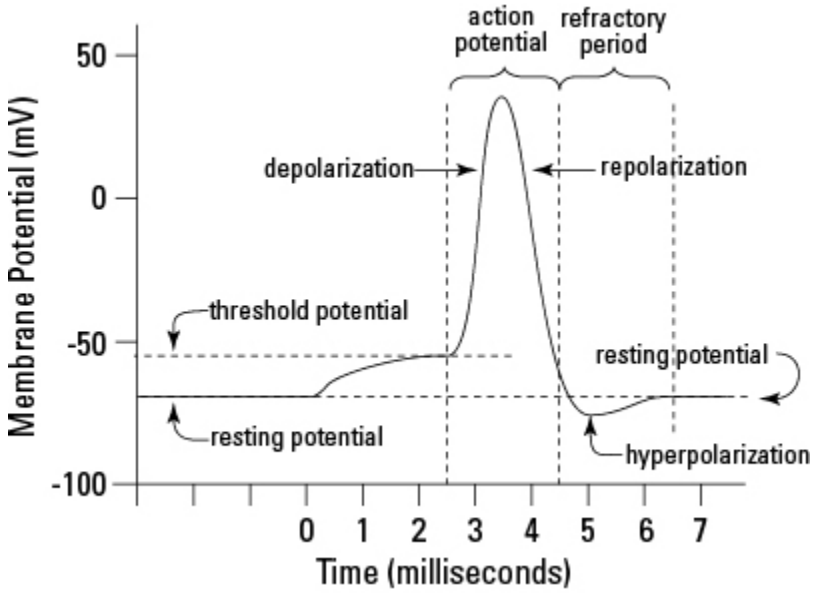

Figure 4: Action Potential Initiation [5]

Once an action potential is initiated at one point in the nerve cell axon, its peak value now will be about +30 mV inside with respect to the outside. Unlike charges attract, so the positive charge will move to the adjacent region of unmyelinated axon causing it to depolarize. As it depolarizes sufficiently, sodium channels in the adjacent region of the membrane will be opened and a new action potential will be initiated [9]. This charge distribution will then spread to the next region causing the action potential to propagate along the axon. During the recovery period depolarization cannot re-occur, therefore when an action potential starts it triggers further depolarization only in the direction

along the axon in which depolarization has not already occurred making action potential propagation unidirectional [10].

2.3 Neuroimaging Techniques

To study the structure, function and behavior of the brain, methods of investigating brain activity arose which can be divided into two types: anatomical techniques and functional scanning.

2.3.1 Anatomical Brain Imaging Techniques. Anatomical or structural brain imaging are techniques which deal with identifying the different structures of the brain and the diagnosis of large-scale intracranial disease such as tumor and injuries [11]. Some examples of structural brain imaging methods are: computed tomography and magnetic resonance imaging.

Computed tomography, also known as CT scan, is a noninvasive anatomical imaging technique that produces multiple images of the bodily organs using x-rays. Different body parts absorb the x-rays in varying degrees. This difference in absorption allows the body structures to be distinguished from one another on the CT electronic image. An advantage of CT is its ability to image bone, soft tissue and blood vessels at the same time in detail [12]. Therefore, CT scanning is suitable for providing anatomic images of head injuries, stroke, brain tumors and other brain diseases as opposed to regular radiographs (x-rays). However, CT does not show the functional aspect of the different brain regions.

Magnetic resonance imaging (MRI) uses a strong external static magnetic field and radio waves to examine organs and their structures. MRI scans are used in diagnosis of various conditions such as tumors [13]. However, like CT, MRI scans do not indicate functions associated with different brain regions.

2.3.2 Functional Brain Imaging Techniques. Functional brain imaging deals with the brain imaging techniques that permit visualizing brain structure and functionality. These techniques are used for better understanding of electrophysiological, hemodynamic, and neurochemical processes that describe normal and pathological brain functionalities [5]. It is widely used in cognitive psychology research as it allows the information processing in the brain to be directly visualized

[11]. There are two types of functional neuroimaging namely hemodynamic and electromagnetic neuroimaging which are discussed below.

Hemodynamic functional neuroimaging is one that monitors the metabolic activity and blood flow within the brain. *Functional magnetic resonance imaging* (fMRI) uses magnetic resonance (MR) imaging to measure the metabolic changes that take place in an active part of the brain. This enables the examination of the anatomy of the brain while monitoring which part of the brain is handling critical functions such as thought, speech, movement, and sensation; this is called brain mapping (Figure 5) [13]. This is performed by the fMRI subtraction method where images from two behavioral conditions are subtracted from each other to yield regions of brain activity. The spatial resolution of fMRI is relatively high of around 3-6 mm. However, its temporal resolution is in the order of seconds which is not sufficient to distinguish between the activation patterns associated with different stages of the rapid stimulus processing. This is due to hemodynamic lag which is 3-6 seconds due to the slow flow of blood through the brain [15].

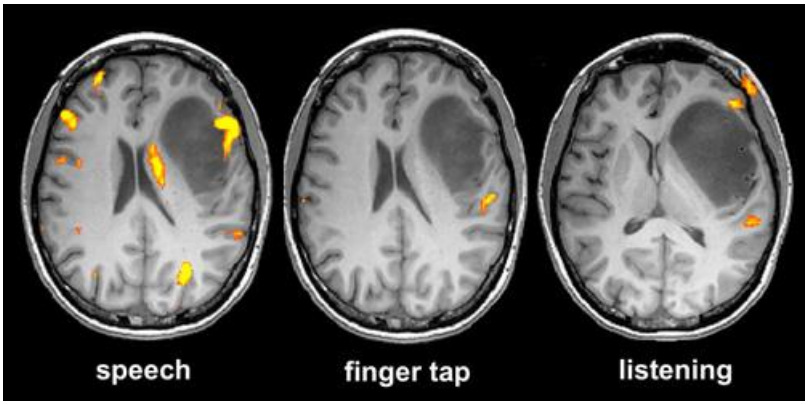

Figure 5: Function magnetic resonance images (fMRI) of active brain areas when subject in engaged in speech (left), finger tap (middle) and listening (right) (Source: http://www.mayfieldclinic.com/PE-fMRI_DTI.htm)

Positron emission tomography (PET) uses small amounts of radioactive materials called radiotracers to help evaluate organs and tissue functions by identifying body changes at the cellular level such as blood flow, oxygen use, and glucose metabolism [12]. A radioactive material is injected into the subject. PET radioisotopes emit a positron, a positively charged electron, in the process of decay. When this positron collides with an electron, they produce 2 photons traveling in opposite directions. This induces electromagnetic radiation which can be detected

externally and is used to measure the quantity and the location of the positron emitter [15]. This is useful in disease diagnosis as seen in Figure 6. PET scans have a spatial resolution of about 4mm throughout the brain but a highly degraded temporal resolution of 30-40 seconds. The invasive nature of PET scans and its low temporal resolution makes it unattractive in real-time applications such as vigilance monitoring.

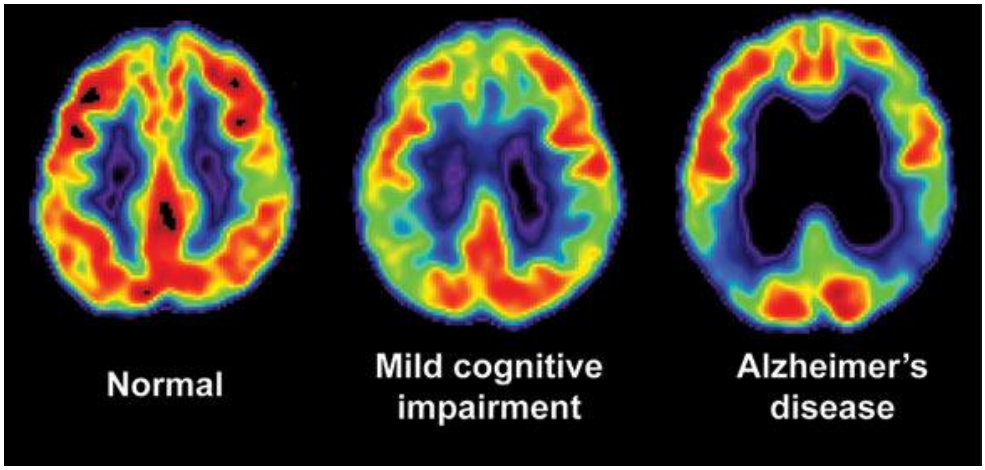

Figure 6: Positron emission tomography (PET) scans for disease diagnosis (Source: http://cognitiveconsonance.info/tag/pet-scan/)

Electromagnetic functional neuroimaging deals with monitoring the electromagnetic activity within the brain. When neural networks fire in synchrony due to a stimulus, the electromagnetic activity can be detected and recorded outside the skull (Figure 7). This is due to the post-synaptic intracellular current flow along the dendrites of pyramidal neurons in the cerebral cortex [15], [16]. Electromagnetic neuroimaging includes magnetoencephalography (MEG) which measures magnetic fields and electroencephalography (EEG) which measures electric potentials.

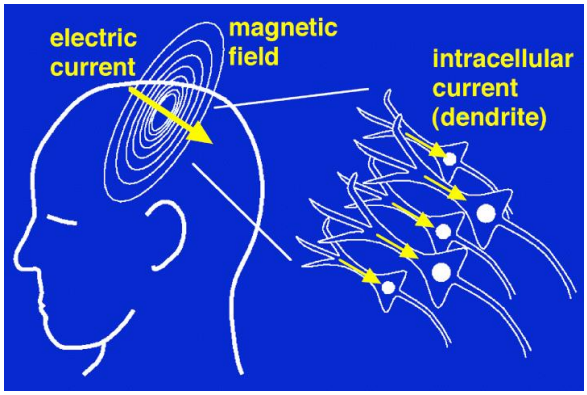

Figure 7: Electromagnetic activity due to intracellular currents [15]

Both MEG and EEG have excellent temporal resolution in the order of milliseconds compared to other neuroimaging techniques (Figure 8), however their spatial resolution is low which requires intense algorithms to localize activated areas in response to a particular stimulus.

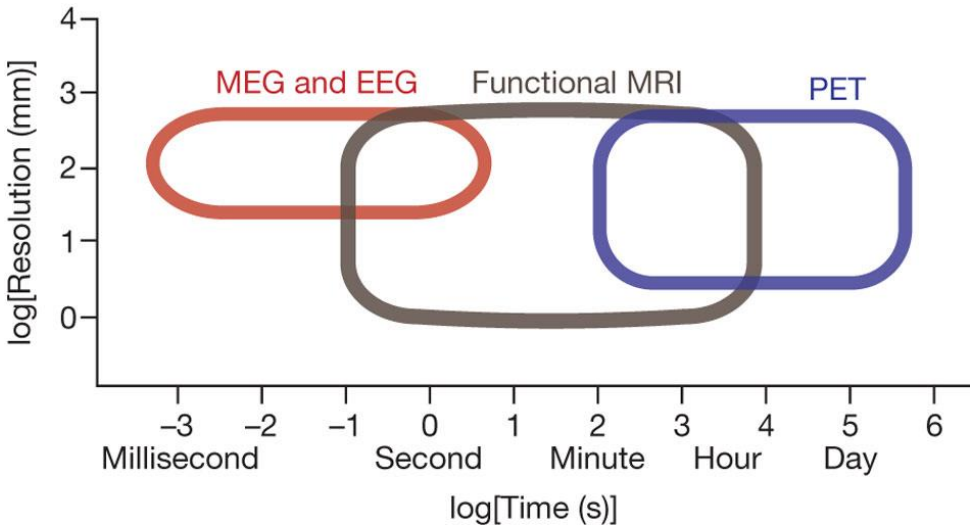

Figure 8: Spatial versus temporal resolutions of functional neuroimaging techniques in logarithmic scale (Source: http://www.nature.com/nature/journal/v468/n7321/fig_tab/nature09569_F1.html)

An MEG signal is dominated by currents oriented tangential to the skull while currents oriented perfectly radial to the skull are missed. However, EEG signals represent tangentially and radially oriented currents equally [15]. The advantage of MEG over EEG signals is that they are more immune to inaccurate head conductor models, however implementation of MEG as a system requires the subjects to not move and the setup is not portable and more complex than EEG systems. Therefore, in this report EEG neuroimaging technique is utilized to study the spatiotemporal behavior of the brain under varying vigilance levels.

2.4 Electroencephalography

Electroencephalography (EEG) is a noninvasive electrophysiological monitoring method that records electrical activity of the brain by measuring scalp electrical potential differences using sensors called *electrodes* as seen in Figure 9.

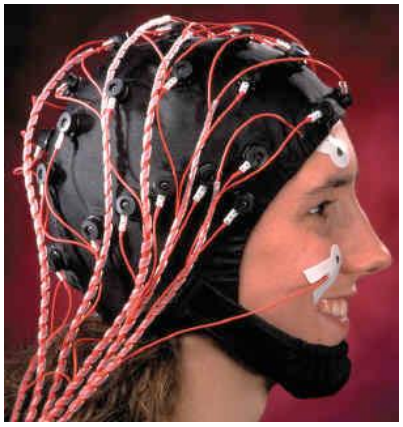

Figure 9: EEG Electrode Setup [15]

Electrode are labelled according to adjacent brain areas: F (frontal), C (central), T (temporal), P (posterior), and O (occipital). The letters are accompanied by odd numbers for electrodes on the left side of the head and even numbers for electrodes on the right side [16]. When neural networks fire simultaneously, electrical activity can be measured outside the brain producing an *electroencephalogram* (Figure 10).

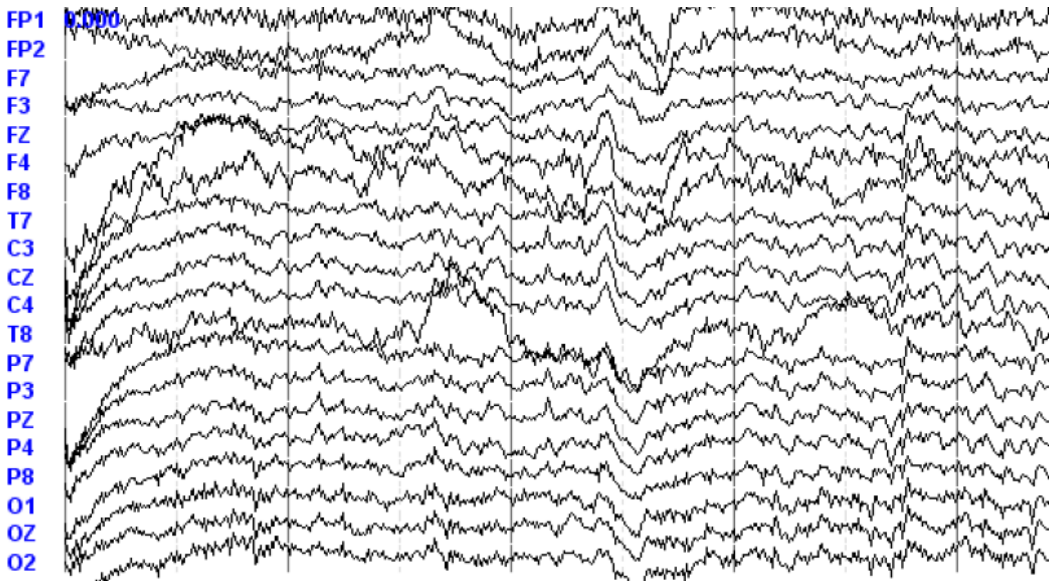

Figure 10: Electroencephalogram recording of the brain

2.4.1 Brain waves. The spectral content of the EEG or *brainwaves* that are observed in EEG signals give indications about diagnosis to brain-related activity. Brainwaves are divided into bandwidths to describe their indications. Brainwaves change according to states of consciousness. Low frequency brainwaves are dominant in states of tiredness, rest, or dreamy. The higher frequencies are dominant in hyper-

alert states and increased cognitive activity. Four main brainwaves (Figure 11) dominate the brain activity: delta δ, theta θ, alpha α and beta β.

Delta waves (δ) are those of frequencies between 0.1 – 4 Hz. They are the slowest brainwaves but have high amplitudes. They are usually generated in deepest meditation and dreamless sleep [17]. They are also involved in unconscious bodily functions such as regulating heart beat and digestion [18].

Theta waves (θ) are in the frequency range 4 – 8 Hz occur most often in daydreaming and sleep. It is also associated with inhibition of elicited responses and a state of somnolence with reduced consciousness [19]. Creativity, emotional connection, intuition, relaxation are some states related to theta waves [18].

Alpha waves (α) are in the frequency range 8 – 12 Hz. Alpha is the resting state for the brain which mainly occurs during quietly flowing thoughts. Alpha waves aid overall mental coordination, calmness and alertness [17].

Beta waves (β) are in the frequency 12 – 30 Hz range. They are high frequency low amplitude brainwaves that are commonly observed when awake [18]. Beta brainwaves dominate our state of consciousness when attention is directed towards cognitive tasks. Beta is present when alert, attentive, engaged in problem solving, and involved in focused mental activity [17].

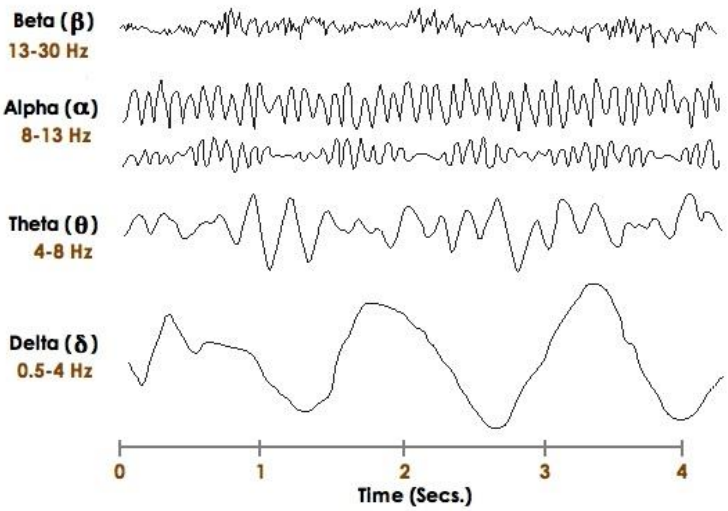

Figure 11: Types of brainwaves (Source: https://sccpsy101.com/home/chapter-2/section-8/brain_waves-3/)

2.4.2 Event Related Potentials. An event-related potential (ERP) is a useful EEG characteristic, which involves averaging the EEG activity time-locked to the presentation of a stimulus such as: visual, somatosensory, or auditory stimuli as in Figure 12.

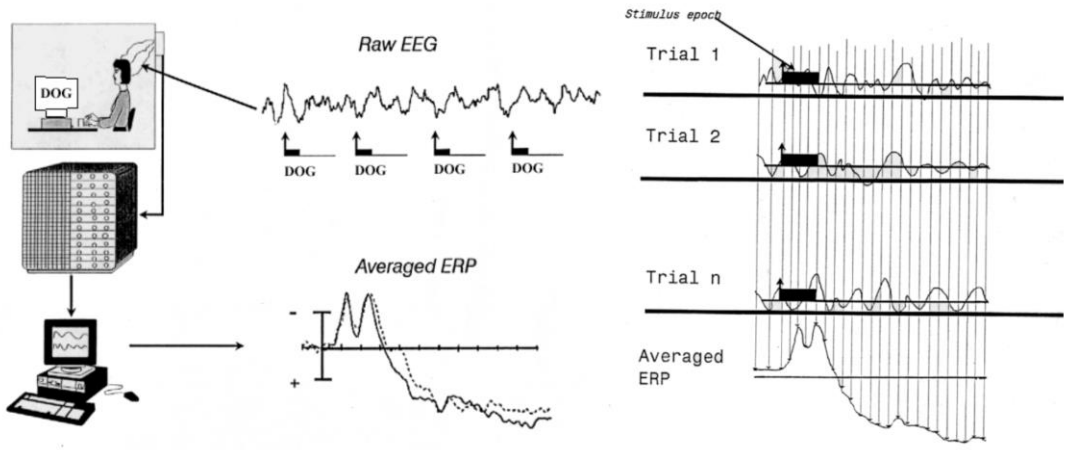

Figure 12: Averaging EEG data to obtain ERP [15]

ERP waveforms are described in terms of positive and negative peaks where typically negative peaks are plotted up and positive peaks are plotted down. The labeling of an ERP starts with a P or a N indicating the peak polarity followed by a number indicating the latency which is the time from stimulus onset. For example, “N100” or ‘N1’ is used to describe an ERP negative peak that occurs 100 milliseconds following stimulus onset as shown in Figure 13.

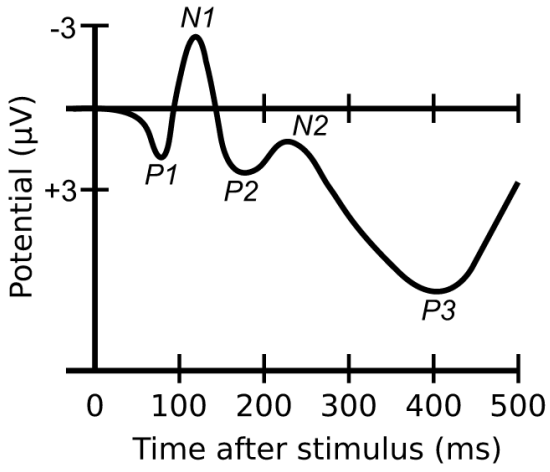

Figure 13: Event-related potential (ERP) Components (Source: http://www.wikiwand.com/en/Event-related_potential)

Functional descriptions of the ERPs identify the cognitive processes reflected by each peak. Additionally, ERP descriptions include the potential brain sources of observed activity. The *P1* or *P100* is an ERP component that is not easily identified. This component is usually interpreted as a neurophysiological indicator to reflect the general level of arousal [20]. It is largest over the occipital regions. The amplitude of P1 generally varies with the amount of attention [20]. *N1* or *N100* is easily identified and is believed to reflect selective attention to basic stimulus characteristics. It largest over the occipital region or the inferior temporal regions. N1 amplitude is typically larger in stimulus discrimination tasks but is reduced when the stimuli are presented at short intervals. However, increased amplitude is attributed to enhanced processing of the attended location but not to arousal. The *P3* or *P300* is the component which arises where a target stimulus is presented infrequently among more common non-target stimuli. The subject must pay attention and respond for a P300 to be elicited [20]. Additionally, the ratio of target to non-target stimuli must be low to get a more visible peak. One factor that affects the P300 amplitude is attention, making it attractive to studies of populations with attention deficits.

2.5 Attention and Brain Function

Attention is fluctuating state of mind where the brain can concentrate on one aspect of the environment while ignoring others. These aspects can be internal such as thoughts or external stimuli such as visual, auditory, and other sensory stimuli. Willful concentration in the brain is believed to reside in the prefrontal cortex with neural activity at low frequencies for intentional work, whereas undeliberate attention is mostly located in the parietal cortex with higher frequencies for automatic processing [21].

The prefrontal cortex is the control center for most cognitive functions where it takes charge of attention in the brain and controls relevant parts of the brain accordingly. A part of the prefrontal cortex known as the inferior frontal junction (IFJ) controls visual processing areas that are responsible for recognizing a specific category of objects [22]. The researchers suggest that the IFJ holds onto the idea of the object and directs the responsible part of the brain to look for it. A study on mice in a cross-modal task, involving visual and auditory senses where they are trained to respond

based on specific cues, suggest that the prefrontal cortex modifies activity in areas of the thalamus to shift attention towards visual information [23].

Some human studies based on event-related fMRI, reported the role of the lateral prefrontal cortex in attentional selection of objects [24]. While others showed that ventral and orbital prefrontal lesions caused deficits in learning new visuomotor associations and retaining pre-learned visuomotor associations [24]. Some scientists suggest that the prefrontal cortex is shown to interact with the inferior temporal cortex in associating a visual stimulus with an action in a conditional visuomotor task [24]. Nevertheless, due to the associative nature of attention function, numerous studies have reported the participation of multiple cortical areas in attentional processes. It has been difficult to localize the exact source of attentive behavior in the brain.

Chapter 3: Monitoring and Measuring Vigilance Decrement Techniques

Various vigilance monitoring methods have been developed recently to combat the penalties of vigilance decrement in critical daily tasks such as driving and surveillances. Some of these methods and their findings are discussed in this chapter.

The authors of [25] used eye tracking techniques by monitoring saccadic eye movements to demonstrate the raise in cognitive workload by observing the changes in the normalized average peak saccadic velocity. Based on a 16-subject experiment where subjects were exposed to a degradation of visual stimuli thus increasing workload. Subjects' saccadic eye movements were monitored as they went through four cognitive workload levels where they were to identify target image sequences from non-target image sequences. They observed that the mean saccadic velocity increases with cognitive workload. They suggest that such method can find application in assessment of vigilance. However, human's visual characteristics vary greatly with factors such as age, height, health, and shape of face [26]. Therefore, saccadic eye movements solely may not produce reliable vigilance assessment results.

By combining eye tracking with EEG data analysis, the authors in [27] study the effect of integrating challenging stimuli with monotonous tasks to enhance vigilance. In the experiment, 12 subjects were asked to watch various activities on the screen and react to a target appearing by pressing a button. The experiment was divided into three phases where phases 1 and 3 induced vigilance decrement due to monotony, while an added noise to the screen in phase 2 made the task more challenging. The eye tracking data comprised of samples with time stamp, pupil size, eye position and eye velocity recorded at a sampling rate of 500Hz. EEG data was collected, and relative band power was calculated to estimate vigilance changes. It was observed that upon introducing the challenging stimuli, the relative delta band power of EEG was suppressed on the fronto-parietal and occipital cortices. Additionally, frontal midline theta power and frontal theta to parietal alpha power ratio increased. 9 out of 12 subjects presented lower relative delta power at phase 2 where vigilance was enhanced. The saccade amplitude and saccade velocity obtained from the eye tracking data are shown to decrease with vigilance decrement, while blink rate increases with vigilance decrement. The reverse trend is observed upon challenge integration.

The authors of [28] designed a monotonous task to induce vigilance decrement across 12 subjects. Accordingly, they extract multifractal attributes of EEG data using wavelet leaders and select the most statistically significant attributes in classification of vigilance into two classes or two vigilance levels: high vigilance and low vigilance. They vary the time window used for feature extraction to improve classification accuracy. They suggest that multifractal attribute features, rather than the conventional power spectral density features, are feasible to differentiate vigilance levels. Finally, they explore the spatial distribution of self-similarity attribute and found that the most difference between the two vigilance levels appear on the frontal and the occipital cortices. This explore the topographies of the averaged multifractal attributes (self-similarity) for the high and low vigilance states, respectively. The difference topography is obtained by subtracting self-similarity values of low vigilance state from that of high vigilance state. The self-similarity is shown to be higher on the frontal cortex and lower on the occipital cortex during high vigilance state.

An EEG-based BCI system is proposed in [29] with a reduced number of EEG channels based on individual variability in EEG. They first collect multi-channels raw EEG signals labeled in two distinct vigilance states. The spectral power in the delta δ, theta θ alpha α and beta β and their ratios $(\theta+\alpha)/\beta$, α/β, $(\theta+\alpha)/(\alpha+\beta)$, and θ/β are calculated as features for vigilance classification. Fisher score is the utilized to remove redundant features and reduce indiscriminative channels. Then, a vigilance model is constructed using a Gaussian Mixture Model (GMM) clustering to assess a gradual vigilance changing process. Parameters, including mean and covariance, of K cluster model are estimated. The number of clusters K represent the resolution of the vigilance level; that is for a sophisticated classification of vigilance K is set to be a large value. However, this method claims that channel reduction is based on individual variability making it impractical when constructing a common vigilance model.

Another approach of using classification in vigilance detection is presented in [30] where EEG data acquired from subjects performing a sleep task is divided into wakeful and sleepy states. Principle Component Analysis (PCA) algorithm is used to reduce 62 channels data to 26 principle components. They propose making use of several channels to extract useful features and utilize the personal feature to construct a self-adaptable vigilance model to eliminate individual differences. The spectral power

in the delta δ, theta θ alpha α and beta β and the ratios (θ+α)/β, α/β, (θ+α)/(α+β), and θ/β are used as features for discriminating vigilance levels. For a specific band or ratio, every principle component's fisher score is calculated to discriminate the significant differences between sleepiness and wakefulness. Using Support Vector Machine (SVM) classification, it was observed that 7 out of 9 subjects showed higher θ band power in the central cortex at the sleepy state, while the α band power is lower in the occipital and parietal cortex and β band power is lower in the frontal cortex. The ratios θ/β and α/β are lower at the sleepy state in the parietal cortex, and α/β is lower in the occipital and temporal cortex. The ratio (θ+α)/(α+β) in the entire cerebral cortex is higher at sleepy state. According to their findings, in the frontal cortex the most difference is found in the δ band and the (θ+α)/(α+β) ratio. In the temporal cortex, the significant difference is found in the δ and α bands and the (θ+α)/(α+β) and α/β ratios. In the parietal cortex, the significant difference is found in the δ and α bands and the θ/β and α/β ratios. In the occipital lobe, the significant difference is found in the β bands and the θ/β ratio.

In [31], the authors propose a single EEG-channel system for detecting low vigilance states during flights. They initially collected two channel derivations (C3-M2) and (O1-M2) for 14 pilots during long-haul flights. The spectral power was calculated for the δ, θ, α and β bands and their ratios relative to the total EEG power. They then performed classification by comparing the normalized value of the relative power of moving windows. They classify a greater relative θ and α power or a lower relative β power than a threshold as a sleepy state. The threshold, λ, was set automatically using a fixed 60 s window recorded before the flight where the pilot is asked to stay seated, quiet and awake with eyes opened. A membership function, defined using the theory of fuzzy sets, is used to classify into sleepy or awake states. The performance level of the algorithm was compared to the results obtained by the classification performed by two experts for 1000 different λ values and the true positive rate (TPrate) was plotted in function of false positive rate (FPrate). They conclude that the (θ+α)/β ratio in the O1-M2 channel provide the best classification.

Chapter 4: Brain Source Localization

EEG signals reflect neural activity in real time leading to its high temporal resolution. However, EEG signals are measured on the surface of the scalp, thus they do not indicate where the brain activity is. Source localization algorithms were formulated to use EEG signals to localize and possibly reconstruct the signal emitted from the specific brain region.

A mathematical model that describes the electromagnetic activity of the brain is developed where the head is modeled as a conductive sphere. Firing neurons are modeled as current dipoles by making use of volume conductor head models assumed to have a specific current density configuration that produces the EEG signals, this is called the *forward problem.* Because we have the scalp potentials while the specific current densities are not available, a-priori assumptions are made to estimate the sources that generated that specific EEG signal pattern and their locations; this is known as the *inverse problem.*

4.1 Forward Problem

The forward problem involves computing scalp potentials given a specific neural activity configuration which is modeled as [32]:

$$V_{ij} = \int L_{ij}^{M}(r).J^{P}(r)dV \quad (1)$$

Where V_{ij} denotes the potential difference measured between electrodes *i* and *j*. $L_{ij}^{M}(r)$ is the leadfield for electrode pairs *i* and *j* which is dependent on the location and configuration of the electrodes and is expressed in Ω/m. $J^{P}(r)$ represents the current density originating from a source at location r and is expressed in A/m^2. For a given current density and a known leadfield matrix a unique solution for the electric potentials can be obtained making the forward problem well-posed.

4.1.1 Neural Generation of Electromagnetic Fields. Considering Maxwell equations for the electromagnetic field:

$$\nabla \times E = -\frac{\partial B}{\partial t} \quad (2)$$

$$\nabla \times H = \frac{\partial D}{\partial t} + J \quad (3)$$

Where $\boldsymbol{E}$ is the electric field intensity (V/m), $\boldsymbol{B}$ is the magnetic flux intensity (W/m^2), $\boldsymbol{D}$ is the electric flux intensity (C/m^2), and $\boldsymbol{H}$ is the magnetic field intensity (A/m).

Since EEG signals are below 1 kHz, quasi-static approximation can be applied to the Maxwell equations by eliminating time dependency such that equation (2) become as follows:

$$\nabla \times E = 0 \tag{4}$$

Taking the divergence of both sides of (3) while eliminating time dependence:

$$\nabla.(\nabla \times H) = \nabla.J \tag{5}$$

Leading to the following:

$$\nabla.J = 0 \tag{6}$$

The total current density $\boldsymbol{J}$ produced by the neural activity which compromises of primary current $\boldsymbol{J_P}$ density generated by neural activity in neurons which is to be localized and secondary currents or return currents $\boldsymbol{J_\Omega}$ that flows passively in the conductive medium:

$$\boldsymbol{J} = \boldsymbol{J_P} + \boldsymbol{J_\Omega} \tag{7}$$

where the return currents $\boldsymbol{J_\Omega}$ can be represented as:

$$\boldsymbol{J_\Omega} = \sigma\,\mathbf{E} \tag{8}$$

4.1.2 Neural source modeled as a current dipole. The coherent activation of a large number of individual neurons in a small volume of the brain can be accurately modeled as a current dipole localized to one site [33].

Neural activity in a small area of the cortex modeled as a current dipole with charge $\boldsymbol{Q}$ at $\boldsymbol{r_Q}$ can be considered as a concentration of primary currents $\boldsymbol{J_p(r)}$ to a single point [32]:

$$\boldsymbol{J_p}(\boldsymbol{r}) = \boldsymbol{Q}\,\delta(\boldsymbol{r} - \boldsymbol{r_Q}) \tag{9}$$

Due to the quasi-static approximation in (6), by using the identity of the electric field expressed in terms of scalar potential $\boldsymbol{E} = -\nabla V$ then applying divergence to both sides of (7), the primary currents can be expressed in terms of the potential:

$$\boldsymbol{\nabla}.\boldsymbol{J_p} = \boldsymbol{\nabla}.(\sigma\,\nabla V) \tag{10}$$

Equation (10) can be solved for V either numerically with finite element techniques or analytically in special cases under proper boundary conditions [32].

4.1.3 Head models are volume conductor models that explain the propagation of the currents through the head in terms of geometry and conductivity [34]. Accurate representation of the forward problem necessitates proper modelling of head geometry and conductivity properties of the head tissues. Mathematically, these properties are expressed in the leadfield matrix. To solve the *inverse problem*, this leadfield matrix is multiplied with the estimated sources or the current density vector to produce the scalp potentials, the *forward solution* [35]. Some common head models used are:

Single Sphere Model is the simplest form of head model where the head is modeled as a sphere with uniform conductivity assumed across the head. However, despite the simplicity and ease of calculation of this model, its source localization accuracy is very limited. A spherical head model estimates the location of the seizure with error up to 2-3 cm [36].

Multiple Spheres Head Model as its name suggests is a model which divides the head to multiple concentric spheres where each sphere has homogeneous conductivity. This model was developed to overcome the shortcomings of single sphere model. The return currents associated with primary currents were used to fit spherical head models for individual MEG sensors to produce a more realistic head model as a set of overlapping spheres, rather than a single sphere [35]. A three-sphere head model considers three layers representing the scalp, skull, and brain. Each layer is assumed to have homogenous conductivity. Multiple spheres head model is considered a more accurate representation of the head model compared to a single sphere head model. Sphere shaped head models are computationally efficient in forward problem formulation and estimation since they allow using analytical solutions [34].

Realistic Head Model yields increased accuracy in modelling head geometry by tessellation of the head compartments from anatomical MRI images [37]. The forward problem is solved using Boundary Element Method (BEM) approach and surface meshes are used to obtain piece-wise homogenous head models. That is, BEM uses *planer* triangular tessellations of the interfaces between sections of equal isotropic conductivities as a geometric model [35]. Another method used in obtaining realistic

head models is Finite Element Method (FEM). FEM solves the forward problem using *volume* tetrahedrons meshes to approximate anisotropy properties of tissue conductivity [35]. In contrast to BEM, the FEM tessellates the whole head volume not just the surfaces thus considering individual, anisotropic conductivities for each element [35].

4.2 Inverse Problem

The inverse problem involves constructing a model with infinitely many degrees of freedom using a finite set of data. Hence, the inverse problem has no unique solution as there are countless models that can explain the data equally. In EEG source localization, the inverse problem constitutes the estimation of sources of neural activity from a given set of potentials. Source localization typically works by first finding the scalp potentials that would result from assumed dipoles or current distribution by solving the forward problem and obtaining the leadfield matrix. Then the inverse problem is solved by using the actual measured EEG data to work back and estimate the sources that fit these measurements. EEG source localization is ill-posed since many source configurations in the brain can produce the same scalp potentials. Given that the number of unknowns is much larger than the number of sensors or electrodes, the problem is severely underdetermined, and regularization methods are essential to restrict the range of allowable solutions [38].

4.2.1 Mathematical Formulation. Assuming multiple dipole sources, due to the principle of superposition, an electrode positioned on the scalp at position vector $\boldsymbol{r}$ will have a potential $m(\boldsymbol{r})$ of:

$$m(\boldsymbol{r}) = \sum_i g\left(\boldsymbol{r}, \boldsymbol{r}_{d_i}, \boldsymbol{d}_i\right) = \sum_i g\left(\boldsymbol{r}, \boldsymbol{r}_{d_i}\right) \boldsymbol{d}_i \tag{11}$$

where $i = 1, \ldots, p$ dipoles and $g\left(\boldsymbol{r}, \boldsymbol{r}_{d_i}, \boldsymbol{d}_i\right)$ is the potential at electrode positioned at $\boldsymbol{r}$ due to a single dipole moment $\boldsymbol{d}_i$ and $\boldsymbol{d}_i = (d_{ix}, d_{iy}, d_{iz})$ is a vector consisting of the three dipole magnitude components [39]. The potential calculated is the referenced potential either to another electrode or an average reference. For *N* electrodes and *p* dipoles and T discrete time samples:

$$\mathbf{M} = \begin{bmatrix} m(\boldsymbol{r}_1, 1) & \cdots & m(\boldsymbol{r}_1, T) \\ \vdots & \ddots & \vdots \\ m(\boldsymbol{r}_N, 1) & \cdots & m(\boldsymbol{r}_N, T) \end{bmatrix} =$$

$$\begin{bmatrix} g(\boldsymbol{r}_1, \boldsymbol{r}_{dip_1})\boldsymbol{e}_1 & \cdots & g\left(\boldsymbol{r}_1, \boldsymbol{r}_{dip_p}\right)\boldsymbol{e}_p \\ \vdots & \ddots & \vdots \\ g(\boldsymbol{r}_N, \boldsymbol{r}_{dip_1})\boldsymbol{e}_1 & \cdots & g\left(\boldsymbol{r}_1, \boldsymbol{r}_{dip_p}\right)\boldsymbol{e}_p \end{bmatrix} \begin{bmatrix} d_{1,1} & \cdots & d_{1,T} \\ \vdots & \ddots & \vdots \\ d_{p,1} & \cdots & d_{p,1} \end{bmatrix} = \mathbf{GD} \tag{12}$$

where **M** is the matrix of data measurements at different time samples, **G** is the leadfield matrix which describes the current flow for a given electrode through each dipole position $\boldsymbol{r}_{dip_i}$ with orientation $\boldsymbol{e}_i$. Each column of **G** relates a dipole to the array of electrode measurements. **D** is the matrix of dipole moments to be localized at different time samples. Dipole moments are assumed to be normal to the surface due to the normal orientation of apical dendrites to the surface which produce the magnetic field [39]. This reduces the elements of the dipole matrix **D** to merely dipole amplitudes. Equation (12) expresses the measurements as an explicit function of primary current activity whereas the passive volume currents due to the macroscopic electric fields are implicitly embedded in the lead field matrix [40].

Considering that the recorded scalp potentials are perturbed with noise, an additive noise matrix **n** is added to the measurements matrix **M**:

$$\mathbf{M} = \mathbf{GD} + \mathbf{n} \tag{13}$$

The inverse problem involves finding an estimate of the dipole magnitude or current distribution matrix $\widehat{\mathbf{D}}$ given the measurements matrix **M** and using the matrix **G** calculated in the forward problem.

4.2.2 Source localization methods. Two approaches for localization are generally used: parametric techniques and non-parametric techniques.

Parametric methods, also referred to as *equivalent current dipole* methods, concentrated source or spatiotemporal dipole fit models, the number of dipoles are assumed to be fixed whose location and orientation are unknown. Since the location and orientation are to be estimated the problem is non-linear. These models vary in complexity from a single dipole in a spherical head model, to multiple dipoles in a realistic head model [39]. Some parametric methods are discussed below.

Non-linear Least-Squares Source Estimation is the earliest and most straightforward method which minimizes the squared error between the measured data and the potentials computed from the estimated hypothetical sources using the forward model. Each dipole represented in matrix $\mathbf{G}$ is associated with six parameters: three location parameters (x, y, z), two orientation parameters (elevation and azimuth angles); and one amplitude parameter. To solve this optimization problem, non-linear minimization of the cost function $\left\|\mathbf{M}-\mathbf{G}\left(\{\boldsymbol{r_j}, \boldsymbol{r_{dip_i}}\}\right)\boldsymbol{D}\right\|$ ($\boldsymbol{r_j}$ is position of electrode $\boldsymbol{j}$) over all the parameters $\left(\boldsymbol{r_{dip_i}}, \boldsymbol{D}\right)$ [39**]**. For p dipoles, the measure of fit in the least-square (LS) sense as the square of the Frobenius norm is:

$$\boldsymbol{J_{LS}}\left(\{\boldsymbol{r_j}, \boldsymbol{r_{dip_i}}\}, \boldsymbol{D}\right) = \left\|\mathbf{M}-\mathbf{G}\left(\{\boldsymbol{r_j}, \boldsymbol{r_{dip_i}}\}\right)\boldsymbol{D}\right\|_F^2 \tag{14}$$

A trivial but highly computationally demanding approach to solving (14) is to use a non-linear search program to minimize $\boldsymbol{J_{LS}}$ over all parameters $\left(\boldsymbol{r_{dip_i}}, \boldsymbol{D}\right)$ simultaneously. However, to reduce the computational burden we select any $\boldsymbol{r_{dip_i}}$ which describes all six parameters associated with a dipole $\boldsymbol{i}$, the matrix $\boldsymbol{D}$ that will minimize $\boldsymbol{J_{LS}}$ is:

$$\widehat{\boldsymbol{D}} = \boldsymbol{G}^{+}\mathbf{M} \tag{15}$$

where $\boldsymbol{G}^{+}$ is the pseudoinverse of $\mathbf{G}$. The adjusted cost function in (13) can be then be minimized to solve for $\boldsymbol{r_{dip_i}}$:

$$\boldsymbol{J_{LS}}\left(\{\boldsymbol{r_j}, \boldsymbol{r_{dip_i}}\}\right)=\|\mathbf{M}-\mathbf{G}(\boldsymbol{G}^{+}\mathbf{M})\|_F^2 \tag{16}$$

The LS problem can be optimally solved in the limited set of non-linear parameters embedded in $\boldsymbol{r_{dip_i}}$ with an iterative minimization procedure. Using (15), the linear parameters in $\boldsymbol{D}$ are estimated.

When the least-squares model is applied to the whole block of data, the dipole locations are fixed over the entire interval; this is called the "fixed dipole' model. However, when the least-squares model is applied sequentially to a set of individual time instants it is called a "moving dipole" model, since the location is not constrained. The fixed and moving dipole models are widely used in processing experimental and clinical EEG data [38]. A disadvantage of the LS method is that the number of dipoles must be assumed a-priori. Additionally, increased number of sources may lead to nonconvexity of the cost function risking being trapped in a local minimum [38].

Beamforming Techniques [38], [39], also known as spatial filters are originally developed in radar signal processing applications but have been found as a useful method in EEG source localization. Beamformers perform spatial filtering on data coming from a sensor array (electrodes in EEG setup) to differentiate signals coming from location of interest among other signals. For an N sensor or electrodes array, the output three element vector of the beamformer $\boldsymbol{y}(t)$ represents the neural activity of each dipole $\boldsymbol{d}$ and is computed as follows:

$$\boldsymbol{y}(t) = \boldsymbol{W}^T \boldsymbol{m}(t) \tag{17}$$

where $\boldsymbol{W}^T$ is the $3 \times N$ spatial filtering matrix with rows equivalent to Cartesian axis and $\boldsymbol{m}(t)$ is the signal at the sensor array at time t which corresponds to the discretized rows of the measurements matrix $\mathbf{M}$ in (12). If the location of interest is $\boldsymbol{r}_{dip}$, the spatial filter would ideally be defined to pass only signals with a unity gain within a small distance δ of this location:

$$\boldsymbol{W}^T(\boldsymbol{r}_{dip})\boldsymbol{G}(\boldsymbol{r}) = \begin{cases} \boldsymbol{I}, & \|\boldsymbol{r} - \boldsymbol{r}_{dip}\| < \delta \\ 0, & \|\boldsymbol{r} - \boldsymbol{r}_{dip}\| \geq \delta \end{cases} \tag{18}$$

where $\boldsymbol{G}(\boldsymbol{r}) = [\mathbf{g}(\mathbf{r}, \boldsymbol{e}_x), \mathbf{g}(\mathbf{r}, \boldsymbol{e}_y), \mathbf{g}(\mathbf{r}, \boldsymbol{e}_z)]$ is the $N \times 3$ forward matrix for three orthogonal dipoles at location $\boldsymbol{r}$ having orientation vectors $\boldsymbol{e}_x$, $\boldsymbol{e}_y$ and $\boldsymbol{e}_z$ respectively. In the previous formulation, however, a strong stop-band constraint over the entire brain volume cannot be attained due to inadequate degrees of freedom. Therefore, fixed spatial filter is impractical for this application. Adaptive spatial filtering methods, such as *linearly constrained minimum variance* (LCMV) beamforming have been proposed to overcome this limitation. In LCMV beamforming, nulls are placed at positions of other neural sources at locations other than that of interest ($\boldsymbol{r}_{dip}$); that is δ is set to zero. The LCMV problem can be written as:

$$\min_{\boldsymbol{W}^T} Tr(\boldsymbol{W}^T E[\boldsymbol{m}\boldsymbol{m}^T]\boldsymbol{W}) \quad \text{subject to} \quad \boldsymbol{W}^T(\boldsymbol{r}_{dip})\boldsymbol{G}(\boldsymbol{r}) = \boldsymbol{I} \tag{19}$$

The optimization in (19) minimizes the beamformer output energy $\boldsymbol{W}^T E[\boldsymbol{m}\boldsymbol{m}^T]\boldsymbol{W}$ under the constraint that only the dipole $\boldsymbol{r}_{dip}$ is active at a time. This attenuates the stop band at sources at other locations. The spatial filter that satisfies (19) can be obtained using Lagrange multipliers as shown in appendix of [39]. The obtained filter $\boldsymbol{W}(\boldsymbol{r}_{dip})$ is applied to each of the rows in $\mathbf{M}$ to obtain an estimate of the dipole moment at $\boldsymbol{r}_{dip}$. This approach assumes that any source can be explained as a weighted combination of

dipoles and can produce an estimate of the neural activity at any location by changing $\boldsymbol{r}_{dip}$. An advantage of the LCMV approach, unlike the LS method, is that it does not require any prior assumptions about the number of dipoles as the localization is performed using the spatial covariance of the surface potentials [41]. Furthermore, distributed sources can be identified given adequate signal-to-noise ratio (SNR) [41]. The limitation of LCMV technique is that due to nulling forced by the constraint in (19) might result in partial cancellation of desired signal due to the often-correlated nature of neural activity in different parts of the brain. However, evaluations on real data seem to indicate LCMV based beamforming methods are robust to *moderate* levels of source correlation [38]. Nonetheless, applications such as vigilance decrement assessment usually studies the brain activity in association brain regions which are typically highly correlated.

Signal subspace methods in array processing exploits the Eigen structure of the measured data matrix for localizing multiple sources [42]. These methods process the EEG data prior to performing source localization. Similar to beamforming techniques, the number of dipoles are not required to be known a priori. However, these methods can be more accurate than beamforming methods since they take into consideration the signal noise when performing dipole localization [39].

Multiple signal classification (MUSIC) is one of the commonly studied subspace methods. The advantage of MUSIC is that it provides computational advantages over direct least squares methods in which all sources are located simultaneously. However, MUSIC allows for exhaustive searches over the parameter space for each source in turn which also is more robust than the LS method in the problem of being trapped in local minima when searching for multiple sources over a nonconvex error surface [42].

For the case of fixed orientation dipoles model, a signal subspace is first estimated from the data by finding the singular value decomposition (SVD) of the measurements matrix: $\mathbf{M} = \mathbf{U}\boldsymbol{\Sigma}\boldsymbol{V}^T$. Assuming that the number of sensors N is greater than number of dipoles p, SNR is sufficiently large, and noise is independent and identically distributed (i.i.d), the column vectors of the subspace matrix $\mathbf{U}$ can be divided into signal and noise subspaces. The first p left singular vectors in $\mathbf{U}$ is an orthonormal basis for the subspace spanned by the data, $\mathbf{U}_{\boldsymbol{s}}$. The approximation of $\mathbf{M}$

in terms of signal subspace is given by $\mathbf{M}_s = (\mathbf{U}_s\mathbf{U}_s^T)\,\mathbf{M}$ and $\mathbf{P}_s^{\perp} = \boldsymbol{I} - (\mathbf{U}_s\mathbf{U}_s^T)$ is the orthogonal projector onto the noise subspace. The MUSIC algorithm minimizes the cost function:

$$\boldsymbol{J_{MUSIC}}(\{\boldsymbol{r},\boldsymbol{e}\}) = \frac{\|\mathbf{P}_s^{\perp}\,\mathbf{g}(\boldsymbol{r},\boldsymbol{e})\|^2}{\|\mathbf{g}(\boldsymbol{r},\boldsymbol{e})\|^2} \tag{20}$$

where $\boldsymbol{r}$ and $\boldsymbol{e}$ refer to the dipole position and orientation vectors respectively. The cost function in (20) is zero when $\mathbf{g}(\boldsymbol{r},\boldsymbol{e})$ corresponds to one of the true source locations and orientations $\boldsymbol{r} = \boldsymbol{r}_{\boldsymbol{dip_i}}$ and $\boldsymbol{e} = \boldsymbol{e}_i$, for $i = 1, \dots, p$.

Since errors in the estimate of the signal subspace $\mathbf{M}_s$ restricts localization accuracy of multiple sources, *recursively applied and projected* (RAP) MUSIC was developed to improve the performance of the MUSIC algorithm by forming an intermediate array gain matrix after each located source. It then projects the array manifold and the signal subspace estimate into its orthogonal complement. MUSIC is then applied to find the next source in this reduced subspace [42]. This procedure projects the signal subspace away from the gain vectors corresponding to the sources already found [38].

Non-parametric source localization methods, also called *distributed source models* or *imaging methods*, assume several dipole sources are distributed in the whole brain volume or cortical surface. Dipoles are assumed to have fixed locations and possibly fixed orientation which are set to be normally aligned as mentioned earlier. The amplitudes and direction of these sources are to be estimated. Non-parametric methods are linear since the dipole location is not estimated [39]. Generally, the number of dipoles considered is much larger than the number of electrodes in these methods.

Minimum norm (MN) was developed in [43] as a solution for the inverse problem: minimum norm estimates for the source current distribution. The authors propose that a linear combination of magnetometer leadfields can be used as an estimate for the current distribution in the brain by applying estimation theory to the inverse problem. Similarly, potential measurements on the scalp can be used as they are generated by the same currents generating the magnetic fields outside the head. The linear relationship between the potential measurements $\mathbf{M}$, current distribution $\boldsymbol{D}$ and the lead field $\boldsymbol{G}$ is shown in equation (12), then the shortest current vector required to explain the measurements can be defined as:

$$\widehat{\boldsymbol{D}} = \boldsymbol{G}^{+}\boldsymbol{M} \tag{21}$$

where $\boldsymbol{G}^{+} = \boldsymbol{G}^{\boldsymbol{T}}(\boldsymbol{G}\boldsymbol{G}^{\boldsymbol{T}})^{+}$ denotes the Moore–Penrose generalized inverse.

Although the minimum norm provides good results in terms of resolution it fails to give weight to deep sources. This due to the harmonic solution of the MN minimum norm for EEG/MEG ($\nabla^2\boldsymbol{J} = 0$) as the harmonic functions are maximum at the boundaries of their domain; which in this case is outermost cortex [44]. Furthermore, the MN assumes that the 3D current distribution should have minimum overall intensity which is not necessarily physiologically valid [45]. Therefore, the algorithm favors weak localized patterns thus bypasses deeper sources. Consequently, weighted minimum norm (WMN) methods were proposed which use different weighting strategies to overcome favoring boundary sources in MN [45].

Low resolution electromagnetic tomography (LORETA) is another nonparametric method which computes the current distribution throughout the full brain volume by assuming that the excitation of neighboring neurons is correlated. It selects the solution with a smooth spatial distribution by minimizing the Laplacian of the weighted sources [45]. The inverse problem for the LORETA can be expressed mathematically as:

$$\min_{\boldsymbol{D}} \boldsymbol{F}_{\boldsymbol{W}} = \|\mathbf{M} - \boldsymbol{G}\,\boldsymbol{D}\|^{2} + \alpha\,\boldsymbol{D}^{\boldsymbol{T}}\boldsymbol{W}\boldsymbol{D} \tag{22}$$

In equation (22), the Tikhonov regularization parameter ¸ $\alpha > 0$ is the control parameter used for controlling of relative importance between penalty for being unfaithful to the measurements and a penalty for a large current density norm [44].

The solution is:

$$\widehat{\boldsymbol{D}}_{\boldsymbol{W}} = \boldsymbol{T}_{\boldsymbol{W}}\,\boldsymbol{M} \tag{23}$$

The value of $\boldsymbol{T}_{\boldsymbol{W}}$ can be calculated by:

$$\boldsymbol{T}_{\boldsymbol{W}} = \boldsymbol{W}^{-1}\boldsymbol{G}^{\boldsymbol{T}}(\boldsymbol{G}\boldsymbol{W}^{-1}\boldsymbol{G}^{\boldsymbol{T}} + \alpha\, H)^{+} \tag{24}$$

where H is the average reference operator defined as [44]:

$$H = I_N - \frac{1}{N}1_N 1_N^T \tag{25}$$

where I_N denotes the $N \times N$ identity matrix and 1_N is a $N \times 1$ matrix composed of ones.

LORETA provides smooth and better localization for deep sources with less localization errors but with low spatial resolution and over-smoothed localized images as compared to MN method.

Standardized LORETA (sLORETA) is an extension of LORETA. It is based on the assumption of the standardization of the current density which considers both the variance of the noise in the EEG measurements and the biological variance in the actual signal considered [46]. This biological variance is assumed as independent uniformly distributed across the brain resulting in a linear imaging localization technique having zero-localization error [45]. The mathematical formulation for sLORETA is:

$$\mathbf{F} = \|\mathbf{M} - \boldsymbol{G}\,\boldsymbol{D}\|^2 + \alpha\,\|\boldsymbol{D}\| \tag{26}$$

This function (26) is to be minimized with respect to $\boldsymbol{D}$ for given $\boldsymbol{G}$, $\boldsymbol{M}$ and α.

The solution $\widehat{\boldsymbol{D}} = \boldsymbol{T}\,\boldsymbol{M}$, where:

$$\boldsymbol{T} = \boldsymbol{G}(\boldsymbol{G}\boldsymbol{G}^{\boldsymbol{T}} + \alpha\, H)^{+} \tag{27}$$

The simulations in [46] demonstrate that sLORETA has far better quality with exact localization and zero-error localization as compared with minimum norm. In a Monte-Carlo analysis, comparing WMN, LORETA, sLORETA among other algorithms, showed that sLORETA gives the best solution for different noise levels and different simulated source depths for single source localization, in terms of both localization error and ghost sources [39]. However, for multiple sources, it has low spatial performance with blurred localized images which fails to resolve proximate sources that are simultaneously active.

Focal under determined system solution (FOCUSS) [44], [47] is an initialization-dependent algorithm proposed as a solution to the low-resolution methods mentioned above. It uses a forward model that utilizes a predetermined reconstruction region and assigns a current to each element within that region. It is recursive where the weights are iterated at each step from the solution of previous step. It uses a low-resolution initial estimate which is refined through an iterative process to yield a sparse solution. The weighted minimum norm method dictates the mathematical calculations

for the recursive steps in FOCUSS. The expression for an unknown current element $\boldsymbol{I}$ can be given as:

$$\boldsymbol{I} = \boldsymbol{W}(\boldsymbol{GW})^{+}M \tag{28}$$

where M is a $N\times 1$ vector containing N radial scalp measurements at the EEG sensors and W is a dimensionless $n \times n$ matrix whose diagonal elements are set to be the previous iterative step solution:

$$W_k = \begin{bmatrix} I_{1k-1} & \dots & 0 \\ \dots & \dots & \dots \\ 0 & \dots & I_{nk-1} \end{bmatrix} \tag{29}$$

Where I_{ik-1} represents the ith element of the vector $\boldsymbol{I}$ at the $(k-1)$th iteration, and k is the index of the current iteration step. The next weight matrix can be calculated by multiplying W_{k-1} by W_k.

Compared to true, minimum norm, unbiased minimum norm for near-surface, mid-depth sources and deep source, the FOCUSS algorithm provides better localization capability and can handle non-uniquely defined localized energy sources. Additionally, FOCUSS algorithm got better spatial resolution and is more stable [47].

Source Affine Image Reconstruction (SAFFIRE) is an algorithm based on an iterative minimum mean square estimation (MMSE) formulation. It aims to reduce the vulnerability to initialization bias by employing a matched filter for initialization purpose. It assumes that measurements at N electrodes is a result of superposition of contributions of M sources modeled as current dipoles on an equidistant grid throughout the brain where each source has three spatial components [48]. The MMSE problem is solved by minimizing the cost function:

$$J = E\{\left|\left|\mathrm{D} - \widehat{\mathrm{D}}\right|\right|^2 = E\{\left|\left|\mathrm{D} - \mathbf{W}^{\mathrm{T}}Y\right|\right|^2\} \tag{30}$$

where D is the $3M \times Q$ vector of dipole component strengths, $\mathbf{W}$ is the $N \times 3M$ MMSE filter bank, and $Y = \boldsymbol{G}\mathrm{D} + \mathrm{n}$ is the $N \times Q$ sensor measurements at Q time samples at which active sources are assumed to be stationary. The norms of the columns of the leadfield matrix $\boldsymbol{G}$ are relatively large for regions close to the sensors which causes the biasness of MNE initializations toward superficial sources. SAFFIRE operates in an affine transformed space in which the norm variations are removed, by transforming $\boldsymbol{G}$ by transformation matrix

$$\mathbf{T} = ([\mathbf{G^T}\boldsymbol{G}] \odot \mathbf{I})^{1/2} \tag{31}$$

$$Y = \boldsymbol{G}\mathbf{T^{-1}}T\mathrm{D} + \mathrm{n} = \boldsymbol{G_a}\mathrm{D}_a + \mathrm{n} \tag{32}$$

where $\boldsymbol{G_a}$ has unit column norms and D_a is the dipole strength components scaled by the column norms of $\boldsymbol{G}$.

The cost function in (30) can be minimized by differentiating J with respect to the matrix $\mathbf{W}$ yielding:

$$\mathbf{W} = (E\{YY^T\}^{-1}) = E\{YD^T\} \tag{33}$$

After affine transformation, the MMSE filter bank becomes:

$$\mathbf{W} = (\boldsymbol{G_a}\, E\{\mathrm{D}_a{\mathrm{D}_a}^T\}{\boldsymbol{G_a}}^T + E\{nn^T\})^{-1}\, \boldsymbol{G_a}\, E\{\mathrm{D}_a{\mathrm{D}_a}^T\} \tag{34}$$

where $\boldsymbol{R_n} = E\{nn^T\}$ is the noise correlation matrix, $\boldsymbol{P} = E\{\mathrm{D}_a{\mathrm{D}_a}^T\}$ is the source correlation matrix which is not known *a priori.* An iterative strategy using direction-of-arrival (DOA) estimation approximates (34) as follows:

$$\widehat{\mathbf{W}}(k) = \left(\boldsymbol{G_a}\widehat{\mathbf{P}}(k-1){\boldsymbol{G_a}}^T + \boldsymbol{R_n}\right)^{-1}\boldsymbol{G_a}\widehat{\mathbf{P}}(k-1) \tag{35}$$

where

$$\widehat{\mathbf{P}}(k-1) = \frac{\left[\widehat{\mathrm{D}_a}(k-1){\mathrm{D}_a}^T(k-1)\right] \odot \mathbf{I}}{\mathrm{Q}} \tag{36}$$

In which $\odot$ is the Hadamard product and $\mathbf{I}$ is the identity matrix and $\widehat{\mathrm{D}_a}(0) = {\boldsymbol{G_a}}^T Y$. The dipole component strength estimates at the kth recursion is:

$$\widehat{\mathrm{D}}(k) = \mathbf{T^{-1}}\widehat{\mathbf{W}}^T(k)Y \tag{37}$$

The iteration process is repeated K times where K is chosen to compromise computation time and a stable source distribution solution.

Chapter 5: Experimental Setup

5.1 Task Choice

An experiment that induced vigilance decrement was carried out using a Matlab-generated attention test. As aforementioned, two hypothesis that explain vigilance decrement phenomenon are: the ‘under-load hypothesis’ states that vigilance decrement occurs due to lack of stimulation cause by minimal workload, while ‘resource depletion theory’, states that intense mental workload in a task causes vigilance decrement. In this experiment, the ‘under-load hypothesis’ was taken up to simulate real life applications such as driving, luggage inspection, air traffic control, quality control, and surveillance jobs. To cause vigilance decrement in an underload hypothesis, the subject should experience an event rate lower than 24 events per minute [49]. Additionally, the target events should not exceed 10% of the total events [50]. The Matlab-generated attention test that was chosen for this purpose is the Psychomotor Vigilance Task (PVT) based on weighted evaluation shown in Table 1.

Table 1: Evaluation of different vigilance tests

Method	Accuracy 35%	Ease of Implementation 35%	Time to induce VD 20%	Availability of supporting literature data 10%	Overall Score
Bakan vigilance test	6	7	6	10	6.75
Mackworth clock	8	5	8	7	5.67
Temple abbreviated test	10	7	7	7	8.05
Counting breaths	2	10	10	5	6.7
PVT test	10	8	9	6	8.7

5.2 Task Description

In the PVT experiment, 33 participants are presented with visual numerical targets among other non-targets, and are required to respond to the assigned target by pressing space bar for a span of 20 minutes in phase 1 of the experiment while recording their brain activity. This is to test the hypothesis that a person's vigilance decrement due to performing a repetitive task such as detecting a target may be correlated to physiological data such as EEG recordings. In phase 2 of the experiment, we attempt to raise vigilance by challenge integration where 22 out of 33 subjects are presented with same task but with a noisy screen background for an additional 5 minutes. The interfaces for both phases are shown in Figure 14.

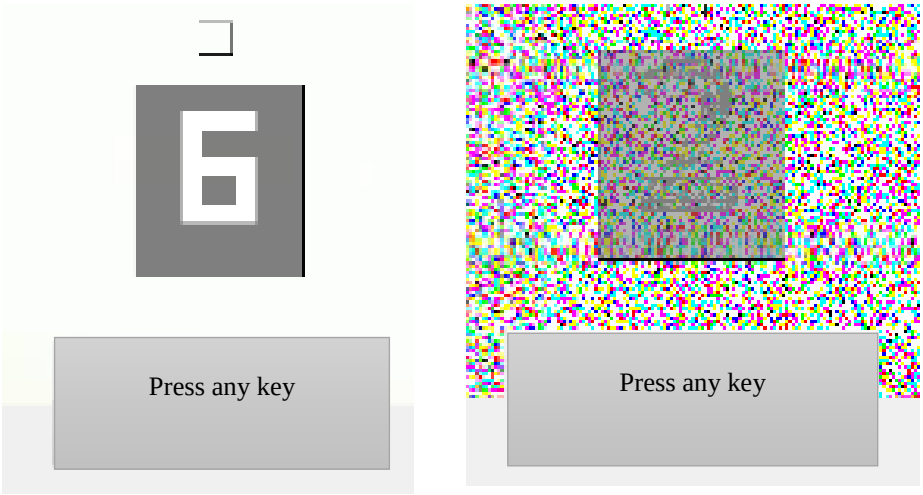

(a) (b)

Figure 14: (a) Phase 1 test interface (b) Phase 2 test interface

The most common causes of vigilance drop are internal and external distractions. The subjects not only suffer from vigilance decrement because of prolonged attention on one task, but also their attention is often shifted to task-unrelated thoughts or activities around them. This highlights the need for adding an element of mild distraction. An audio file was used to serve this purpose by simulating sound distractions occurring in daily life. Nevertheless, the audio is chosen in such a way that the speaker's tone, the topic, and the language used are all not engaging and lack any form of mental stimulation. In this way, the presence of the distraction will have little or no effect on the nature of the resulting EEG signal.

5.2.1 Task Protocol. Numbers from 0 to 9 appear on the screen. Each number appears for 0.4 seconds and then disappears, leaving the blank grey background for 1.6

seconds, and then another numbers appears. This means that 30 numbers appear per minute. The activity lasts for 20 to 30 minutes, making the total number of events occurring per subject equal to 600 to 900. Out of those events, 30 to 40 targets will appear, once every 19 events (5.26% target percentage). The target is number *3*, and the subject is instructed to respond to the target by pressing the space bar as fast as they can, and not to respond to the appearance of any other number. The subject is not given any instructions regarding the audio file. Throughout the task, the subject is listening to the audio file.

5.2.2 Equipment Setup. The equipment used in this experiment is as follows:

- 64 electrode EEG cap
- EEG amplifier
- Two PCs: 1 for the ASAlab software, and 1 for the Matlab-generated test (test terminal)
- ASAlab software (v4.9)
- Matlab-generated PVT attention test on PC

The subject undergoing the experiment was fitted with 64 electrodes EEG cap on the head and the EEG data was recorded at a sampling frequency of 500 Hz using Advanced Source Analysis (ASA) lab software. The subject was also fitted an ECG (electrocardiogram) and an EOG (electrooculogram) electrodes for heart activity and eye movements respectively. The EEG cap is connected to the recording computer through an EEG amplifier. This amplifier is connected to the 64 electrode EEG cap as well as the electrodes 65 and 66 used to measure EOG and ECG signals. The block diagram of the setup is shown in Figure 15.

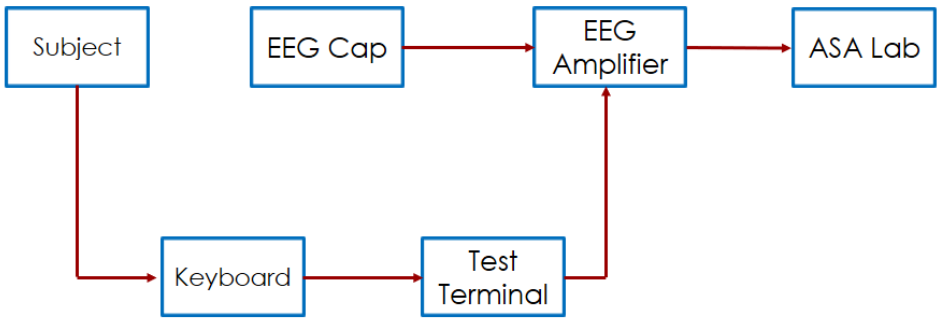

Figure 15: Experiment Setup block diagram

Chapter 6: Experimental Results

6.1 Data Overview

This chapter presents the analysis of the data recorded during the experiment. To identify vigilance decrement of subjects undergoing the attention task behavioral data and EEG physiological data are collected during the experiment for analysis. Behavioral data are obtained from the reaction time, time between the occurrence of the event and the subject's response, using Matlab. In attention tasks where the aim is to identify a target among non-target events, an increase in reaction time or the number of errors is a direct sign of vigilance decrement. The points at which any event occurs, whether a target or a non-target, is marked on the EEG signal along with the time at which a subject responds in order to correlate behavioral data and EEG data.

The reaction time of subjects' response to target stimuli is used as a proof of vigilance decrement concept. *Advanced Source Analysis* (ASA) lab software and *Brainstorm* software were used to study the PSD of the EEG signals by comparing the first and last 5 minutes of the data before challenge integration, which are labeled as awake and drowsy states respectively. Finally, 5 minutes of the challenging task is compared to the other two states. The recorded data is analyzed using two approaches: power spectral density (PSD) and source localization SAFFIRE algorithm.

In PSD approach, the spectral behavior of different brainwaves is compared between awake and drowsy states across different regions of the brain, as well as their relation to the reaction time. Due to the unknown nature of the number of sources in relation to vigilance, nonparametric source localization methods are adopted. SAFFIRE algorithm is chosen as the best candidate for this application due to its iterative nature leading to its high spatial resolution while circumventing initialization bias. The *P300* component among other ERP components mentioned in section 2.4.2 are to be localized for awake, drowsy and challenge states. The source density distribution across the head is compared for both states to construct a vigilance assessment model.

6.2 Data Preprocessing

The recorded unprocessed EEG data comprises of random unwanted signals called *artefacts* (Figure 16) such as eye blinks and eye movements. Accordingly, the EEG signals are preprocessed to remove these artifacts to get a clean EEG signal showing only the brain activity. This can be achieved using the *artefact correction*

feature in ASAlab which corrects the data for artefacts using a Principle Component Analysis (PCA) method by modelling the brain signal and artefact subspaces.

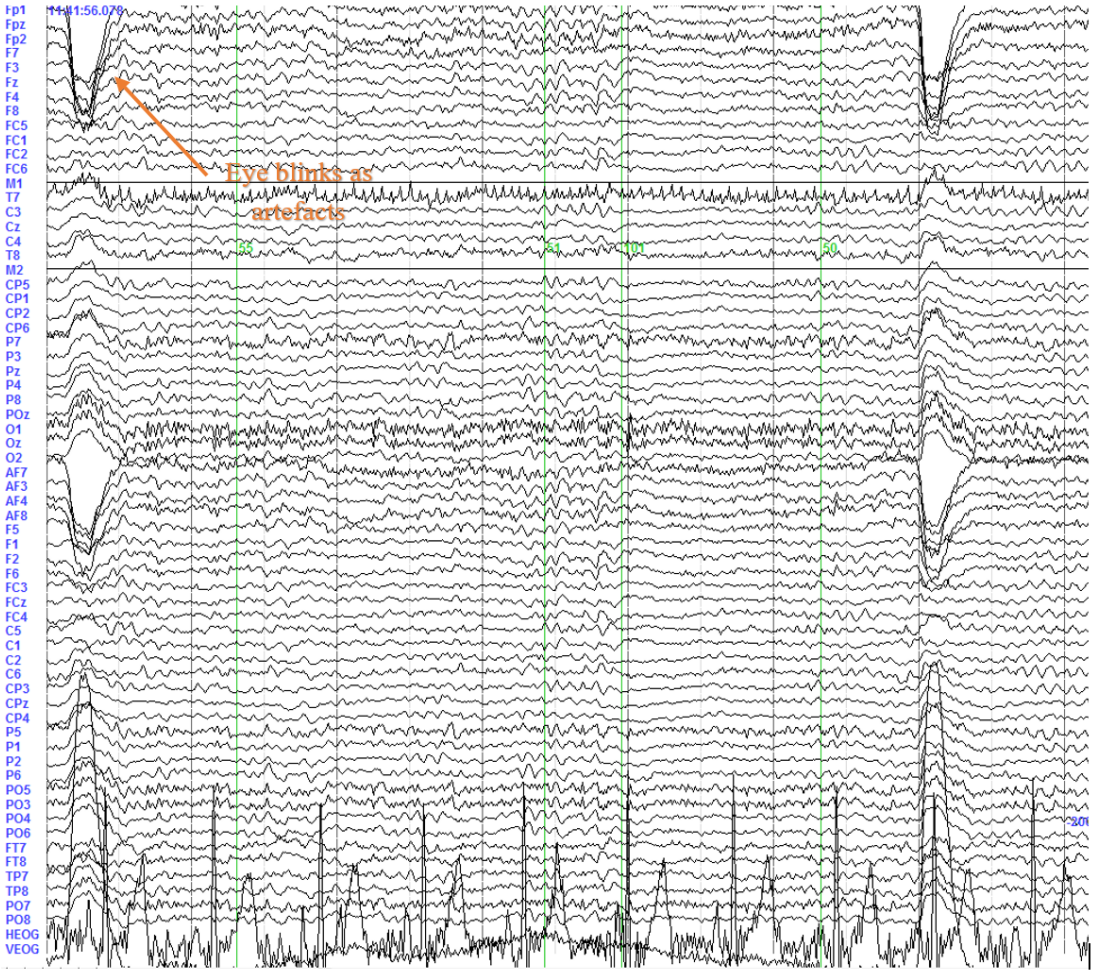

Figure 16: Sample EEG recording before processing

The PCA method separates brain signal from artefacts based on their topographies and subsequently removes the artefacts without significant distortion to the brain signal [51]. The separation is achieved by means of a data interval with a clear artefact activity selected by the user (Figure 17). The marked artefacts should be typical in shape, length, and spatial distribution (electrode channels) to specify the artefact topography. The method determines which part of the data are considered brain signal or data subspace using two criteria. The first criterion specifies the highest permitted amplitude of the brain signal while the second criterion specifies the highest correlation between brain signal and artefact topography permitted. Then, Principal Components Analysis method is used to determine the topographies of the brain activity signals and

the artefact signals, thus removing signal portions with the artefact components leaving a signal with only brain activity (Figure 18).

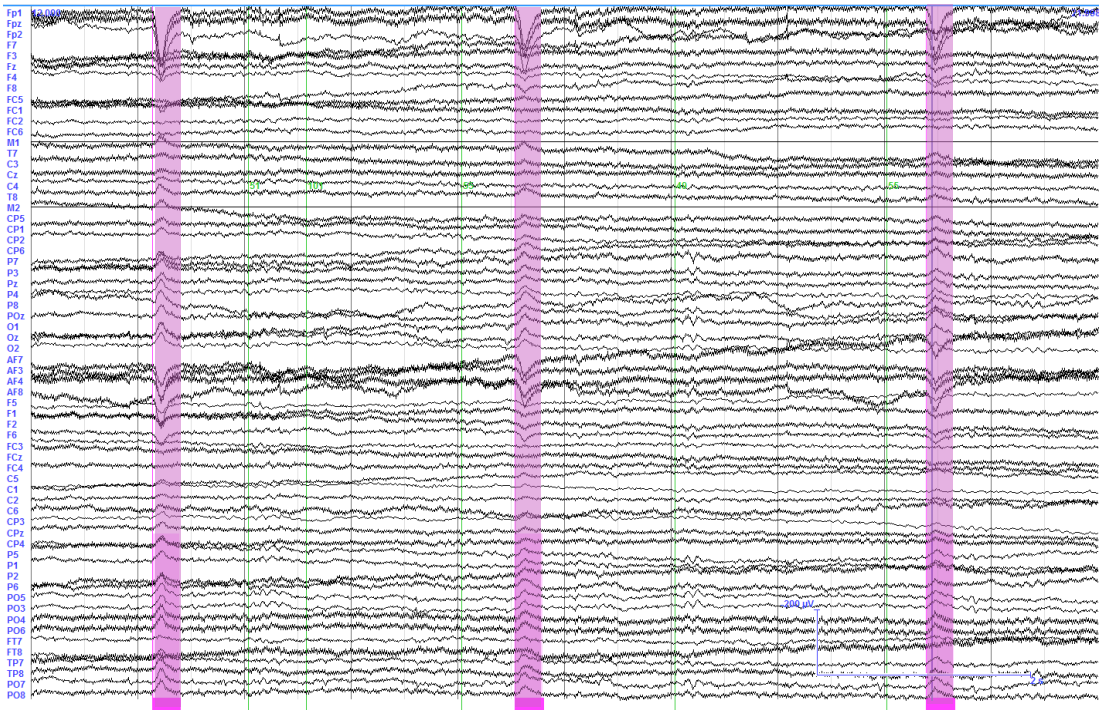

Figure 17: EEG signal with selected artefact events

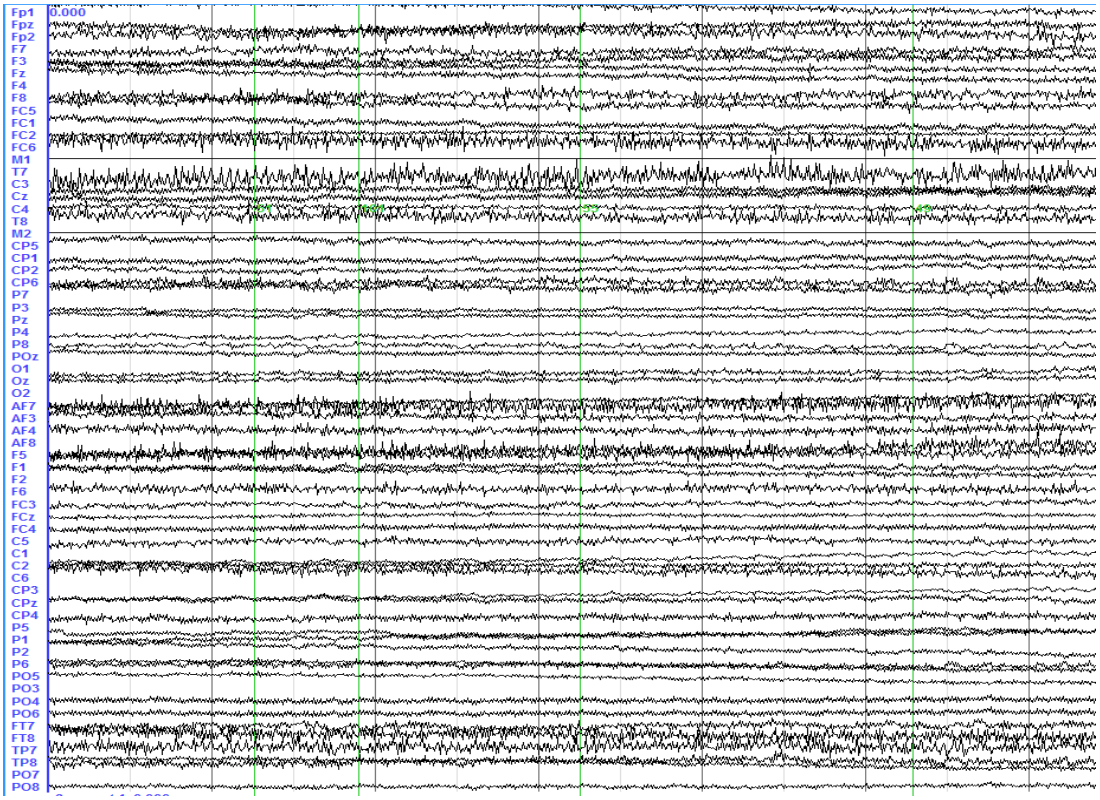

Figure 18: EEG signal after artefact removal

After the artifact removal, EEG signal is passed through high pass and low pass filters in series with cut-off frequencies 0.5 Hz and 30 Hz respectively to get rid of noisy signals outside the band of interest where brainwaves are dominant. Additionally, the EEG signal is passed through a 50 Hz and 150 Hz notch filter to attenuate the mains interference as seen in Figure 19– 21.

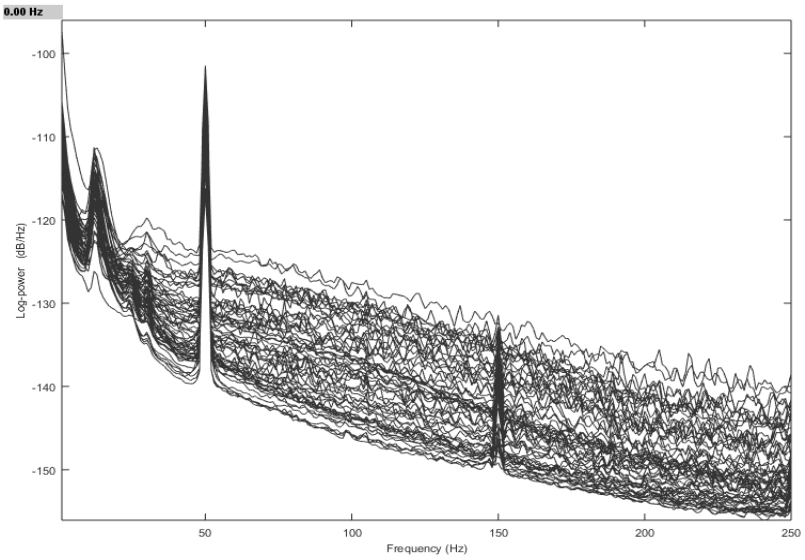

Figure 19: Power spectral density (PSD) of unfiltered EEG signal

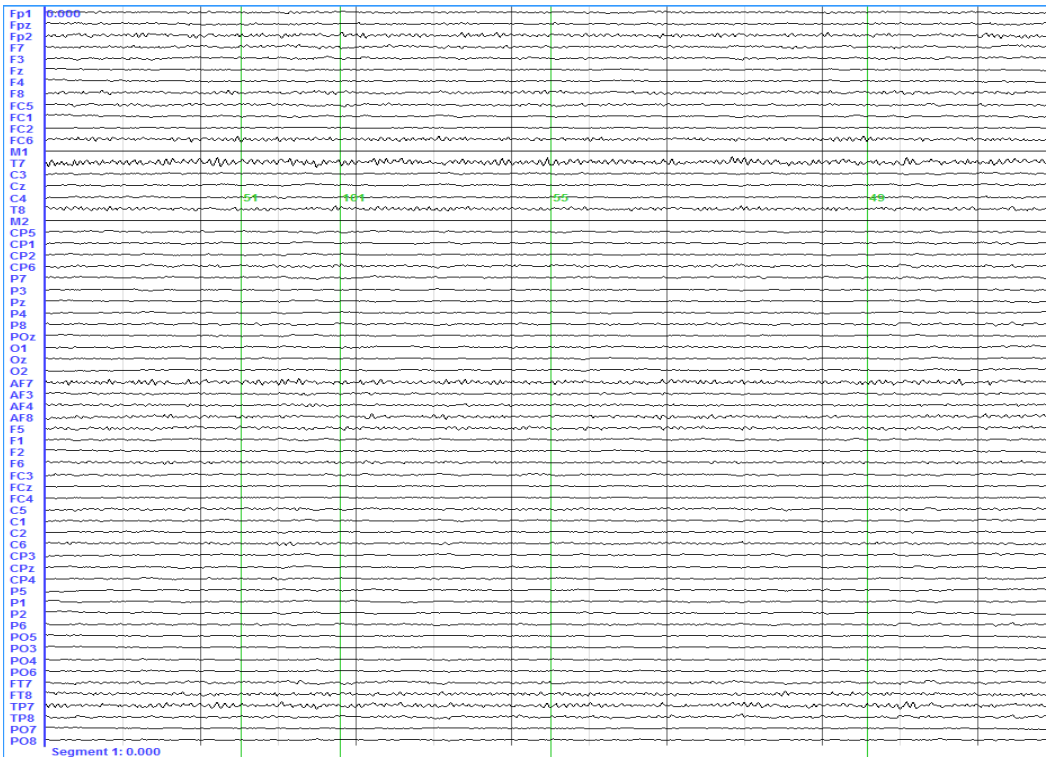

Figure 20: Filtered EEG signal

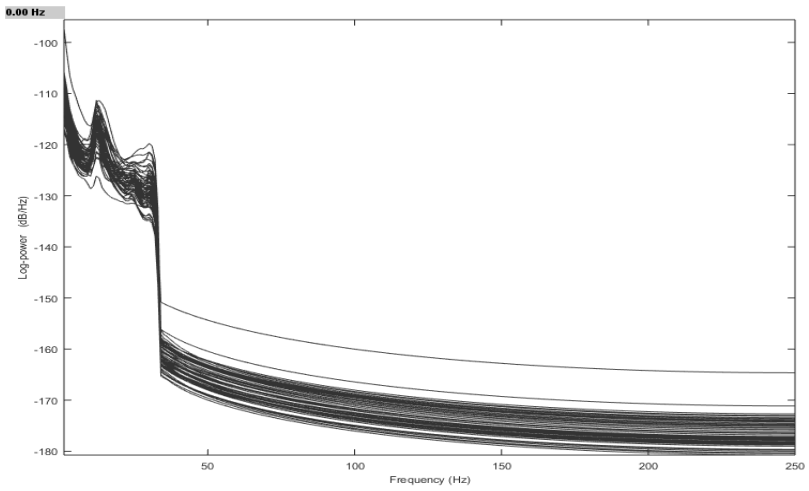

Figure 21: Power spectral density (PSD) of Filtered EEG Signal

6.3 Experimental Vigilance Assessment

In this section, the behavioral data and the preprocessed EEG data are analyzed. First, the average reaction time for all subjects is observed as an indication of success of PVT task in inducing vigilance decrement. Second, two techniques of analyzing changes in the EEG physiological data with vigilance decrement are presented: power spectral density (PSD) and EEG source localization.

6.3.1 Reaction Time. Vigilance decrement can be observed by an increase in reaction time, the time taken to respond to a target stimulus. The reaction time to target stimulus of 22 subjects was recorded during the experiment. The average reaction time among all subjects was plotted against time as seen in

Figure 22. The general trend shows an increase in reaction time as the task progresses.

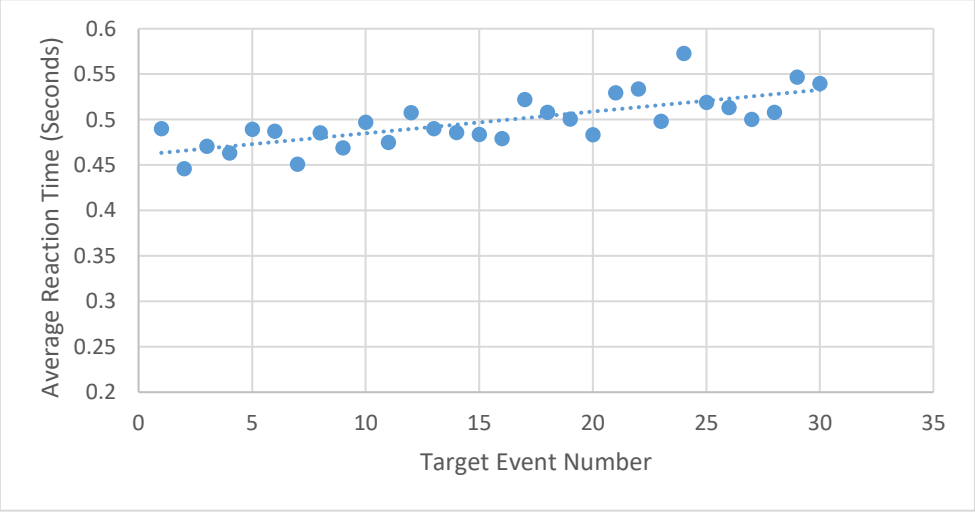

Figure 22: Average reaction time

In order to signify the difference in reaction time between the awake and drowsy states, a Student's paired t-test was performed on the reaction time in the first and last 5 minutes in phase 1 of the task. For each subject, the average reaction time in the first 5 minutes (t_1) and the last 5 minutes (t_2) were calculated and compared using the t-test. The results are summarized in Table 2.

Table 2: Reaction time t-test for awake and drowsy states

$t_2 - t_1$	Hypothesis (h)	p-value
Two-tailed t-test	1	0.0067
Right-tailed t-test	1	0.0034
Left-tailed t-test	0	0.9966

The two-tailed t-test above tests the null hypothesis that the mean difference between t_1 and t_2 is zero. Where the right-tailed t-test tests whether the mean or $t_2 - t_1 > 0$, and the left-tailed t-test tests whether the mean or $t_2 - t_1 < 0$. h = 1 indicates the rejection of the null hypothesis while h = 0 indicates a failure to reject the null hypothesis. The results above show that the mean difference is more than 0 with 0.34 % probability that the null hypothesis is valid. This shows a clear increase in the reaction time for drowsy state.

The reaction time for 10 subjects out of the 22 subjects who participated in phase 2 of the experiment was recorded. A paired t-test is performed between the drowsy state (t_2) and the challenge state (t_3). The results are summarized in Table 3.

Table 3: Reaction time t-test drowsy and challenge states

$t_2 - t_3$	Hypothesis (h)	p-value
Two-tailed t-test	1	0.0367
Right-tailed t-test	0	0.9817
Left-tailed t-test	1	0.0183

The left-tailed t-test shows that $t_2 < t_3$; the mean reaction time for challenge state increased. In [52], the reaction time was shown to increase with increase mental workload. Therefore, this increase could be due to the necessary increase in the

individual's processing of the noisy background thus increasing the time to react in a blurred vision environment.

6.3.2 Power Spectral Density (PSD). The spectral content in the EEG signal has been widely examined in works monitoring vigilance. Fast Fourier Transform (FFT) analysis is performed on processed EEG signals across different electrodes. The head electrode configuration was tessellated into 9 different regions, from which the center electrode was to be analyzed as a reflection of the other electrodes in the region. The electrodes chosen for analysis are shown in Figure 23. These electrodes include: *AF7, Fpz,* and *AF8* which are located on the left, center and right prefrontal region respectively. Electrodes *C5*, *Cz* and *C6* are located on the left, center and right central region respectively. While electrodes *PO5, POz,* and *PO6* are located on the left, center and right parieto-occipital region.

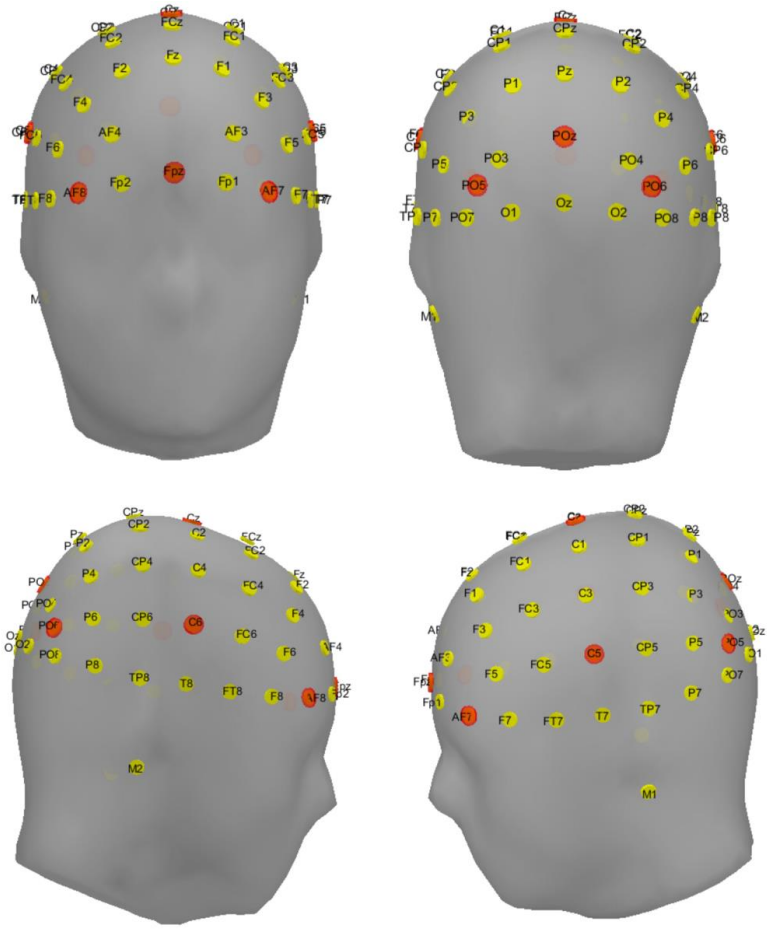

Figure 23: Electrodes chosen for power spectral density (PSD) analysis

For each electrode, the evoked-related potential (ERP) signal for target and non-target events in the awake, drowsy and challenge states is analyzed for power in delta δ, theta θ, alpha α and beta β bands for all subjects. Initially, the null hypothesis is assumed which states that the mean difference band power between states is zero. A paired-sample t-test is then performed across subjects to validate changes in brainwaves power in different brain sensors. To combat noise in EEG signals, event segments are averaged for each state to obtain a clean ERP signal. Two different latencies, 500ms and 1400ms, for averaged ERPs are used to reinforce obtained results and ensure consistency. The null hypothesis is only rejected if both latencies shared the same direction in the t-test with an acceptable p-value, which is chosen to be 0.1. The results are presented in Table 4 – 7.

Table 4: Power spectral density (PSD) analysis for delta band

Electrode	ERP Latency	Target						Non-Target					
		Drowsy – Awake			Drowsy – Challenge			Drowsy – Awake			Drowsy – Challenge		
		h	p-value	Tail	h	p-value	Tail	h	p-value	Tail	h	p-value	Tail
Fpz	500 ms	1	0.052	Right	1	0.091	Right	0	0.116	Right	0	0.195	Left
	1400 ms	1	0.046	Right	0	0.347	Right	0	0.101	Right	0	0.142	Right
Cz	500 ms	0	0.288	Right	0	0.324	Right	0	0.444	Right	1	0.014	Left
	1400 ms	0	0.160	Right	0	0.291	Right	0	0.360	Left	0	0.223	Left
POz	500 ms	0	0.485	Right	0	0.398	Left	0	0.308	Left	0	0.374	Right
	1400 ms	0	0.411	Right	0	0.334	Right	0	0.134	Right	0	0.200	Left
AF7	500 ms	1	0.070	Right	1	0.075	Right	0	0.162	Right	0	0.387	Left
	1400 ms	1	0.027	Right	1	0.043	Right	1	0.029	Right	0	0.144	Right
AF8	500 ms	1	0.023	Right	1	0.005	Right	0	0.459	Right	0	0.247	Left
	1400 ms	1	0.032	Right	0	0.136	Right	0	0.119	Right	0	0.286	Right
C5	500 ms	0	0.269	Right	0	0.121	Right	0	0.195	Left	0	0.252	Right
	1400 ms	0	0.374	Right	0	0.241	Right	0	0.404	Right	0	0.254	Right
C6	500 ms	0	0.160	Left	1	0.022	Right	0	0.274	Left	0	0.148	Left
	1400 ms	1	0.082	Left	1	0.083	Right	0	0.346	Left	1	0.096	Left
PO5	500 ms	0	0.430	Right	0	0.395	Left	0	0.421	Left	0	0.216	Left
	1400 ms	0	0.135	Right	1	0.052	Right	0	0.280	Left	0	0.358	Left
PO6	500 ms	0	0.162	Left	1	0.098	Left	1	0.079	Left	0	0.235	Left
	1400 ms	1	0.017	Left	0	0.471	Left	0	0.432	Left	0	0.240	Right

The delta power shows a significant increase in drowsy state for target events in three electrodes *Fpz*, *AF7* and *AF8* which are located on the prefrontal cortex. While

electrodes *AF7* and *C6* show a lower delta power for challenge state than drowsy state. For non-target events, no consistent trend was shown across the electrodes.

Table 5: Power spectral density (PSD) analysis for theta band

Electrode	ERP Latency	Target						Non-Target					
		Drowsy – Awake			Drowsy – Challenge			Drowsy – Awake			Drowsy – Challenge		
		h	p-value	Tail	h	p-value	Tail	h	p-value	Tail	h	p-value	Tail
Fpz	500 ms	1	0.075	Right	1	0.067	Right	0	0.411	Left	0	0.185	Right
	1400 ms	1	0.019	Right	0	0.234	Right	0	0.150	Left	0	0.358	Left
Cz	500 ms	1	0.100	Right	0	0.179	Left	0	0.406	Left	0	0.201	Left
	1400 ms	0	0.394	Left	0	0.388	Right	1	0.006	Left	0	0.119	Left
POz	500 ms	1	0.085	Right	0	0.126	Right	1	0.004	Left	1	0.054	Right
	1400 ms	1	0.086	Right	1	0.027	Right	0	0.113	Left	0	0.466	Right
AF7	500 ms	1	0.051	Right	1	0.063	Right	0	0.411	Right	1	0.034	Right
	1400 ms	0	0.407	Right	1	0.052	Left	1	0.083	Right	0	0.113	Right
AF8	500 ms	1	0.079	Right	1	0.087	Right	1	0.079	Right	0	0.238	Right
	1400 ms	1	0.011	Right	0	0.466	Left	0	0.155	Right	0	0.460	Left
C5	500 ms	1	0.030	Right	1	0.052	Right	1	0.017	Left	0	0.453	Left
	1400 ms	1	0.035	Right	1	0.096	Right	0	0.123	Left	0	0.343	Right
C6	500 ms	0	0.462	Left	1	0.013	Right	1	0.073	Left	1	0.022	Right
	1400 ms	0	0.364	Left	1	0.098	Right	0	0.316	Left	0	0.390	Left
PO5	500 ms	0	0.104	Right	0	0.364	Right	1	0.067	Left	0	0.230	Right
	1400 ms	1	0.015	Right	1	0.084	Right	1	0.036	Left	0	0.498	Left
PO6	500 ms	1	0.038	Left	0	0.255	Right	0	0.180	Left	0	0.446	Right
	1400 ms	1	0.009	Right	0	0.124	Right	0	0.139	Left	0	0.220	Left

In the theta band, an increase for drowsy state is observed in *Fpz*, *POz*, *AF8* and *C5* electrodes. Additionally, theta decreased for challenge state in the *C5* and *C6* electrodes. Non-target events show a decrease in theta for drowsy state in *PO5* sensor.

Table 6: Power spectral density (PSD) analysis for alpha band

Electrode	ERP Latency	Target						Non-Target					
		Drowsy – Awake			Drowsy – Challenge			Drowsy – Awake			Drowsy – Challenge		
		h	p-value	Tail	h	p-value	Tail	h	p-value	Tail	h	p-value	Tail
Fpz	500 ms	0	0.206	Right	0	0.110	Right	0	0.365	Left	1	0.038	Right
	1400 ms	1	0.038	Right	0	0.198	Left	0	0.280	Right	0	0.191	Right
Cz	500 ms	0	0.200	Right	0	0.411	Left	0	0.181	Left	1	0.077	Right
	1400 ms	1	0.081	Right	0	0.479	Left	0	0.319	Right	0	0.467	Right
POz	500 ms	1	0.094	Right	0	0.412	Right	1	0.038	Left	1	0.013	Right
	1400 ms	1	0.017	Right	1	0.058	Left	0	0.305	Right	0	0.422	Left
AF7	500 ms	1	0.009	Right	1	0.005	Right	0	0.370	Right	1	0.027	Right
	1400 ms	1	0.001	Right	1	0.026	Right	0	0.258	Right	1	0.042	Right
AF8	500 ms	1	0.020	Right	1	0.109	Right	0	0.108	Right	0	0.214	Right
	1400 ms	1	0.022	Right	1	0.084	Right	0	0.259	Right	0	0.304	Left
C5	500 ms	1	0.053	Right	0	0.313	Right	0	0.377	Left	0	0.243	Right
	1400 ms	1	0.002	Right	0	0.189	Left	0	0.435	Left	0	0.300	Left
C6	500 ms	1	0.050	Right	1	0.083	Right	1	0.010	Left	1	0.067	Right
	1400 ms	0	0.264	Right	0	0.443	Right	1	0.083	Left	0	0.329	Left
PO5	500 ms	0	0.370	Right	0	0.388	Right	0	0.255	Left	1	0.024	Right
	1400 ms	0	0.164	Right	0	0.173	Left	0	0.491	Left	1	0.041	Right
PO6	500 ms	0	0.350	Right	0	0.310	Right	0	0.491	Left	1	0.058	Right
	1400 ms	1	0.041	Right	0	0.405	Left	0	0.147	Right	0	0.353	Left

For alpha band, a higher power is observed in drowsy state than the other two states in the *AF7* and *AF8* electrodes. *POz* and *C5* also show an increase in for drowsy alpha in compared to awake alpha, but show no change for challenge state. A decrease in *C6* electrode for drowsy state is observed in non-target events. The electrode *AF7* and *PO5* show a decrease for non-target events in challenge theta power as compared to drowsy state.

Table 7: Power spectral density (PSD) analysis for beta band

Electrode	ERP Latency	Target						Non-Target					
		Drowsy – Awake			Drowsy – Challenge			Drowsy – Awake			Drowsy – Challenge		
		h	p-value	Tail	h	p-value	Tail	h	p-value	Tail	h	p-value	Tail
Fpz	500 ms	1	0.014	Right	0	0.357	Left	0	0.393	Left	0	0.300	Right
	1400 ms	1	0.042	Right	0	0.237	Left	1	0.014	Right	0	0.215	Left
Cz	500 ms	0	0.444	Left	0	0.422	Right	1	0.009	Left	1	0.012	Right
	1400 ms	1	0.101	Right	0	0.217	Left	0	0.239	Right	0	0.115	Right
POz	500 ms	0	0.384	Right	0	0.477	Right	0	0.273	Left	1	0.053	Right
	1400 ms	1	0.070	Right	0	0.197	Right	0	0.237	Right	0	0.136	Right
AF7	500 ms	1	0.010	Right	0	0.411	Left	1	0.066	Right	0	0.169	Left
	1400 ms	1	0.001	Right	0	0.218	Left	1	0.002	Right	0	0.271	Left
AF8	500 ms	0	0.115	Right	0	0.157	Left	1	0.100	Right	0	0.165	Left
	1400 ms	0	0.121	Right	0	0.152	Left	0	0.120	Right	0	0.158	Left
C5	500 ms	1	0.093	Right	0	0.281	Right	1	0.051	Right	0	0.108	Right
	1400 ms	1	0.076	Right	0	0.211	Right	1	0.090	Right	1	0.092	Right
C6	500 ms	1	0.061	Right	0	0.122	Right	1	0.023	Left	0	0.182	Left
	1400 ms	0	0.275	Right	0	0.160	Right	0	0.343	Left	0	0.491	Left
PO5	500 ms	0	0.412	Left	0	0.369	Right	1	0.040	Left	1	0.001	Right
	1400 ms	0	0.200	Left	0	0.147	Left	0	0.123	Right	0	0.233	Right
PO6	500 ms	0	0.396	Left	0	0.225	Left	1	0.006	Left	0	0.214	Right
	1400 ms	0	0.353	Right	0	0.192	Left	1	0.071	Right	1	0.026	Right

Beta power increased in drowsy state for *Fpz*, *AF7* and *C5*. *AF7* and *C5* also show an increase in beta power for non-target events. Change for challenge state is inconsistent.

The electrodes with highest sensitivity to drowsy state in most bands are shown to be the prefrontal electrodes *AF7*, *Fpz*, and *AF8* and left central electrode *C5* as shown in Table 8.

Table 8: Electrode sensitivity analysis

Electrode	Delta	Theta	Alpha	Beta	Total
Fpz	1	1	0	1	3
Cz	0	0	0	0	0
POz	0	1	1	0	2
AF7	1	0	1	1	3
AF8	1	1	1	0	3
C5	0	1	1	1	3
C6	0	0	0	0	0
PO5	0	0	0	0	0
PO6	0	0	0	0	0

6.3.3 Source Localization. In this approach source localization SAFFIRE algorithm is applied to awake and drowsy states for all subjects, where the *P300* component and/or any other ERP components are to be localized. In order to obtain an ERP signal, the EEG signal is to be averaged across all target events. The events in EEG data are labeled with vertical green lines associated with a label number for each distinct event as seen in Figure 24. The labels *51* and *101* represent appearance of the target number and a *true positive* respectively. A true positive event is when the target number appears, and the subject correctly responds to it.

Figure 24: Event labels in EEG signal

We are interested in the brain behavior once it recognizes the target event, consequently, the EEG signal is averaged for awake and drowsy states over the target event appearances labeled as *51*. The resulted signal is the ERP to be localized as seen in Figure 25. This averaging yielded the P300 signal with a latency of around 270 milliseconds in predominantly frontal to parietal electrodes as stated in [53].

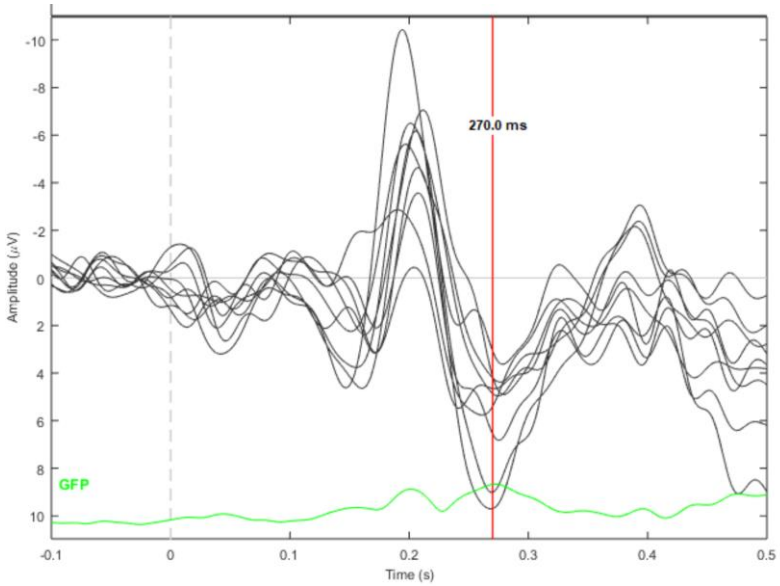

Figure 25: ERP obtained from averaged EEG signal

To perform localization, a realistic volume head conductor model is necessary for an accurate solution of the forward problem; that is the *leadfield matrix*. Using *Brainstorm* software, boundary element method (BEM) was utilized to produce a numerical forward solution that account for the individual shape of the head layers. The BEM was performed on the MRI of the Collins brain (Collins 27 or ICBM 27); which is a standard MRI consisting of 27 T1-weighted scans of the same person. The alternative was to scan the individual MRI head images of all 33 subjects which is infeasible. This head model is used in solving the inverse problem for localizing the ERP signal obtained.

To solve the inverse problem, SAFFIRE algorithm was used to localize averaged ERPs for awake, drowsy and challenge states for each subject. The brain region was tessellated into an equidistant grid with 15000 voxels where a dipole or a source is assumed at each voxel. As aforementioned, dipoles are assumed to be normal to the surface due to the normal orientation of apical dendrites to the surface [39]. This reduces the solution of the inverse problem to merely dipole amplitudes at each voxel.

A tradeoff between computational time and convergence to a stable solution necessitates choosing the number of iterations carefully. A superficial source is assumed in the left prefrontal cortex as show in Figure 26(a). Using the forward problem previously obtained, scalp potentials are computed. SAFFIRE algorithm is used to localize the fabricated scalp potentials, and the number of iterations K= 15 was shown to give an accurate solution as shown in Figure 26(b).

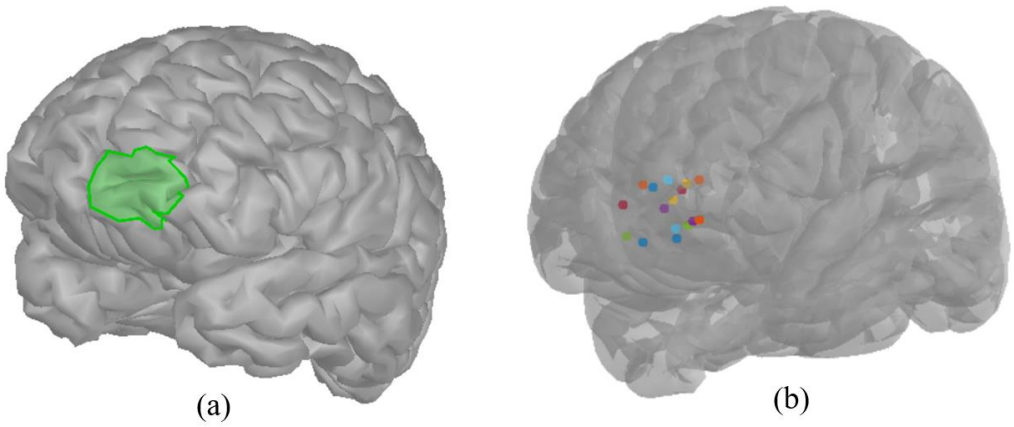

Figure 26: (a) Superficial brain source (b) Localized sources using SAFFIRE algorithm

SAFFIRE algorithm is used to localize averaged ERPs for target events in awake, drowsy and challenge states respectively. The solution yields a power at each of the 15000 voxels. The brain is divided into 7 regions: prefrontal, frontal, central, parietal, right temporal, left temporal and occipital (Figure 27). Accordingly, the magnitude of the powers in each region were added. Two approaches were used; the first, the absolute powers were added within a region for each state and compared using a t-test. Second, the powers across states for each subject were normalized to eliminate subject variability in EEG measurements. The results are summarized in Table 9.

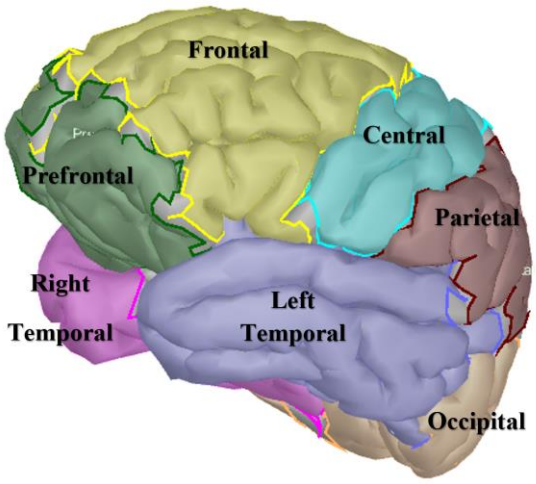

Figure 27: Brain regions for source localization

Table 9: Source localization t-test in different regions

Region	Power Magnitude	Drowsy - Awake			Drowsy - Challenge		
		h	p-value	Tail	h	p-value	Tail
Prefrontal	Absolute	1	0.015	Right	1	0.067	Right
	Normalized	1	0.099	Right	0	0.148	Right
Frontal	Absolute	1	0.020	Right	0	0.131	Right
	Normalized	1	0.008	Right	0	0.462	Right
Central	Absolute	1	0.068	Right	1	0.024	Right
	Normalized	0	0.155	Right	1	0.032	Right
Parietal	Absolute	0	0.138	Left	0	0.173	Left
	Normalized	0	0.101	Left	0	0.153	Left
Right Temporal	Absolute	1	0.084	Left	0	0.318	Right
	Normalized	0	0.248	Left	0	0.115	Right
Left Temporal	Absolute	0	0.211	Right	1	0.088	Right
	Normalized	0	0.482	Left	0	0.202	Right
Occipital	Absolute	0	0.122	Right	1	0.026	Right
	Normalized	1	0.049	Right	1	0.024	Right

As can be seen from Table 9, the prefrontal and frontal areas show a clear increase in power in drowsy state in comparison to awake state. An increase in central region is shown for the absolute power, but is less evident for normalized power. Similarly, occipital lobe shows a slight increase in activity. The parietal region shows a slight decreased activity with p-values 0.138 and 0.101 for absolute and normalized powers respectively. Right and left temporal show inconsistent results for absolute and normalized powers. However, for challenge state the power in central and occipital regions are shown to decrease in comparison with drowsy state which is opposite to the changes in these areas from awake to drowsy states.

For visualization of the number of sources dominant in each state, the powers across subjects were averaged and normalized for all three states. The power greater than 30% of the maximum was projected on the brain as seen in Figure 28. Each point represents a source at the corresponding voxel. It is apparent that the number of sources and their intensity increased in drowsy state, then decreased again in challenge state.

In order to categorize the power distribution for different regions, the power magnitudes' histogram was shown to resemble a *Rayleigh distribution*. The power magnitudes were normalized by 10^{-5} for visualization. The fitted model for awake, drowsy and challenge states are shown in Figure 29. There is a significant shift to the right in the distribution from awake to drowsy state in prefrontal and frontal regions. The central and occipital regions show a slight increase, while the parietal shows a slight decrease in the mean value. The right temporal shows a decrease in activity from awake to drowsy states, while the left temporal shows no change across all states. It is observed that the challenge state distribution is close to that of the awake state; this could indicate the success in inducing vigilance enhancement.

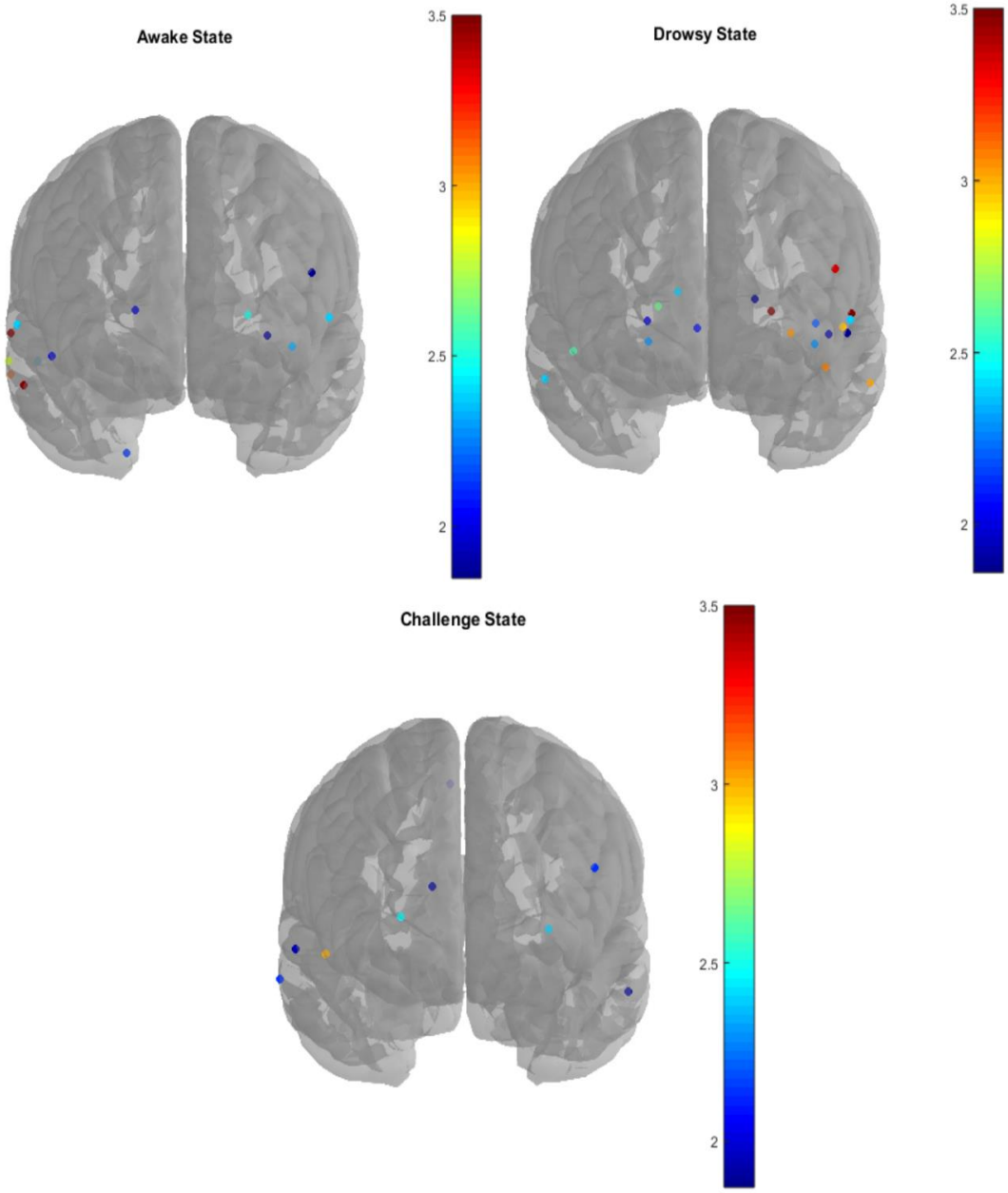

Figure 28: Front view of brain activity: each point represents a source at the corresponding voxel and the dot color represents its normalized power value according to the color map.

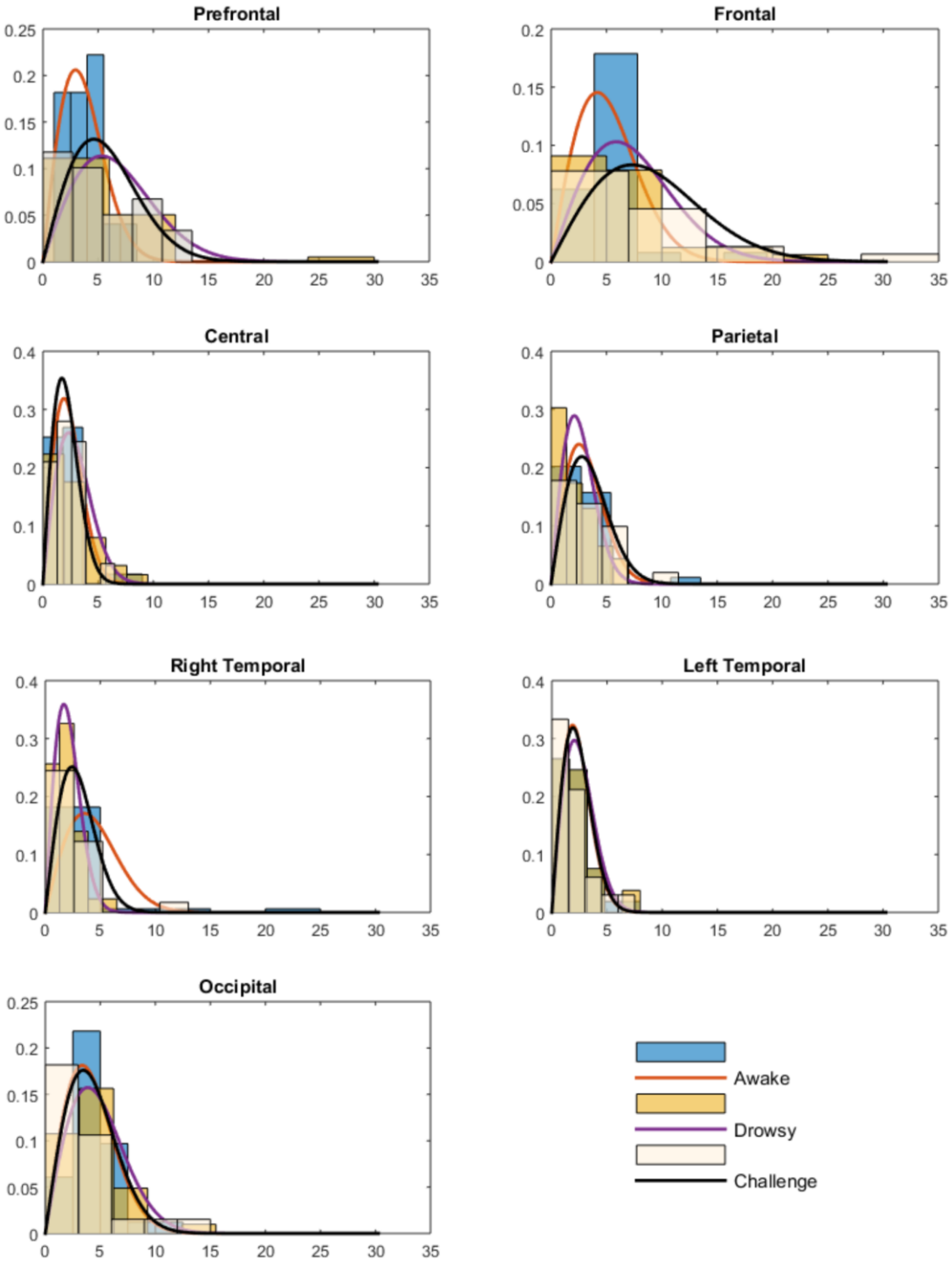

Figure 29: Power probability density function for awake, drowsy and challenge states

6.3.4 Vigilance Measurement Model. To quantify vigilance level, many brain dynamics must be taken into consideration. The significant shifts in the delta, theta and alpha bands along with the clear source dynamics of the prefrontal cortex can be used in conjunction to construct an initial vigilance assessment model.

From previous results, the delta, theta, and alpha brainwaves showed an increase in the *AF8* electrode for drowsy state for both latencies. For these bands, Rayleigh distribution models for target events in awake and drowsy states are fitted for the 500 ms averaged ERP in *AF8* electrode (Figure 30). This latency is chosen to reduce computational time in real-time applications. Power for these bands were normalized by 10^{-12} for proper visualization.

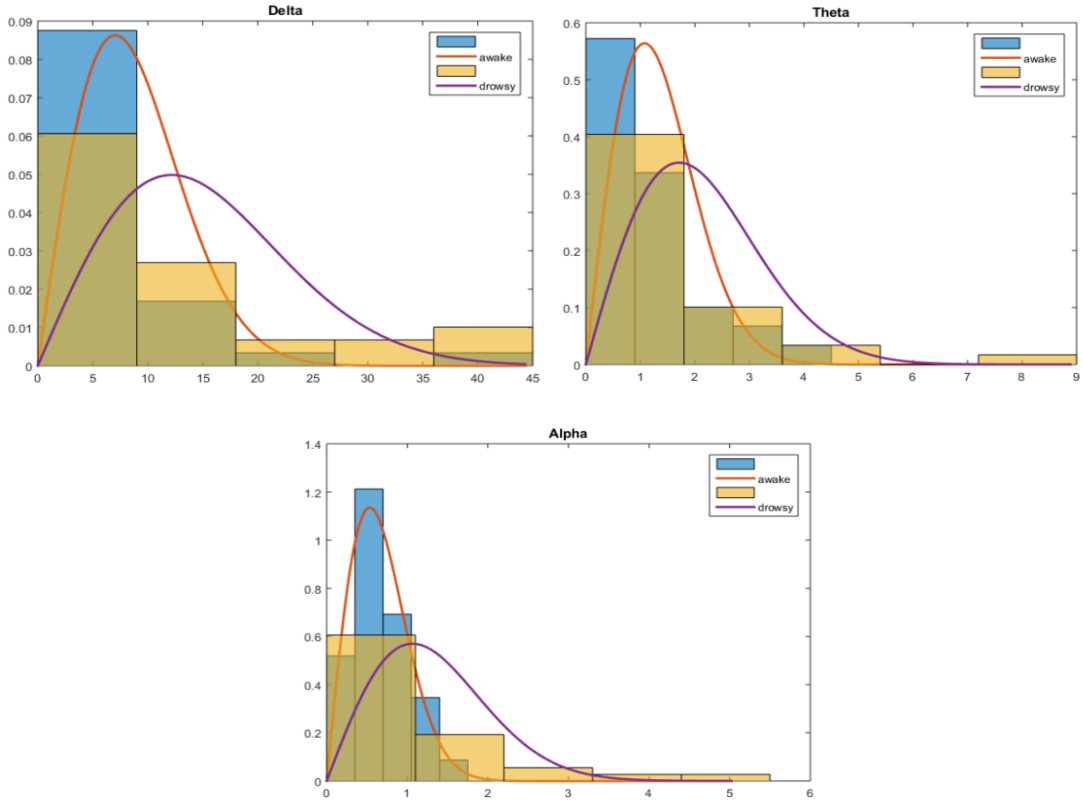

Figure 30: Delta, theta and alpha power probability distribution for awake and drowsy states

The Rayleigh distribution has a probability density function defined as:

$$f(x|b) = \frac{x}{b^2} e^{-\frac{x^2}{2b^2}} \tag{38}$$

Where b is the distribution parameter which is a function of the mean m where

$$m = b\sqrt{\frac{\pi}{2}} \tag{39}$$

The parameters of the Rayleigh distributions above, along with the prefrontal cortex distribution, are summarized in Table 10.

Table 10: Rayleigh distribution parameters for different EEG variables

Variable	b_{awake}	m_{awake}	b_{drowsy}	m_{drowsy}
Delta power (x_1)	7.0318E-12	8.813E-12	1.22E-11	1.5261E-11
Theta power (x_2)	1.08E-12	1.3474E-12	1.71E-12	2.1447E-12
Alpha power (x_3)	5.34E-13	6.6975E-13	1.07E-12	1.3348E-12
Prefrontal magnitude (x_4)	2.94E-05	3.6893E-05	5.34E-05	6.695E-05

In order to assess the vigilance level 1 or 2, awake and drowsy respectively, we must compute the joint probability distribution of the variables for each vigilance level. we can write the probability for vigilance level i as:

$$\mathrm{P}_i(x_1, x_2, x_3, x_4 | b_{i1}, b_{i2}, b_{i3}, b_{i4}) = \frac{x_1 x_2 x_3 x_4}{(b_{i1} b_{i2} b_{i3} b_{i4})^2} e^{-(\frac{{x_1}^2}{2{b_{i1}}^2} + \frac{{x_2}^2}{2{b_{i2}}^2} + \frac{{x_3}^2}{2{b_{i3}}^2} + \frac{{x_4}^2}{2{b_{i4}}^2})} \tag{40}$$

Using maximum likelihood estimation (MLE) we can test for a specific data point for all levels and decide for the one with the highest probability. The decision process is:

$$\mathrm{P}_i > \mathrm{P}_j \text{ for } \forall\, j \neq i \quad \text{we assign the vigilance level } i \tag{41}$$

The above algorithm was performed on the labeled data for awake state where 28 out of 33 subjects (84.85%) were correctly identified to be vigilant.

An assumption that can be made in this model is that the variables' mean values are linear with vigilance decrement. That is, by regression we can assume, for example, that the mean values for the vigilance level 3 is following a Rayleigh distribution with mean linearly spaced from m_2 by $|m_1 - m_2|$ where $m_3 = m_2 + |m_1 - m_2|$. Further experiments with longer task durations can be conducted to validate this assumption.

Chapter 7: Discussion, Conclusions and Future work

7.1 Discussion

The increase in the average reaction time assumes the vigilance decrement phenomena. The results obtained using PSD approach showed an increase in delta δ predominantly in the prefrontal cortex with vigilance decrement which could be due its relaxing nature. Furthermore, delta power decreases again with vigilance enhancement in the *AF7* electrode on the left frontal region of the brain which agrees with findings in [27]. The power in theta band increased across most brain regions with vigilance decrement like results in [27] and [30] . In vigilance enhancement phase, the theta power decreased specifically in central regions, *C5* and *C6* electrodes. The similarity between awake and challenge states, suggest that vigilance is associated with lower delta and theta powers. In [54], lower arousal state is linked to higher amplitudes in low frequency waves delta and theta. The electrodes that show reliable trends in delta and theta powers are *AF7* and *C5* respectively.

A lower alpha is also observed in *AF7* and *AF8* electrodes in awake and challenge states, which increases with vigilance decrement in frontal areas. A study, indicated that alpha waves can be used to predict errors, where MEG measurements showed up to 25% increase in alpha waves before a mistake occurred [55]. After the subjects noticed the mistake, they started paying more attention to the task where a decrease in alpha waves was observed [55]. The logic behind this observation could be that alpha waves are associated with calmness and are prominent when a person starts doing a task automatically without paying much focus. The power for beta band increased in left frontal and central areas in *Fpz, AF7* and *C5* electrodes. A possible explanation for this increase is the increase in mental effort required while experiencing vigilance decrement. Narcolepsy patients experienced an increase in beta power due to exerting more effort to do normal daily functions [56]. Beta power is associated with cognitive functions demanding higher allocation of attentional resources. There is a possibility that vigilance decrement causes a depletion of these resources for prolonged obligatory simple tasks.

The source localization method shows an increase in prefrontal and frontal region activities with vigilance decrement. The increase in the overall power could account for the higher brain waves powers, as well as the association of increased

prefrontal activity with increases in mental workload [57]. Previous fMRI, Transcranial Doppler sonography (TCD), lesion and split-brain studies suggest that the control of vigilance resides in the right frontal cortex [57], [58]. In figure 28, the increase is shown to be more noticeable in the left frontal region which could mean that despite the increased sources in drowsy state, the brain is ineffective in utilizing the right frontal region for higher vigilance control. Studies investigating brain areas responsible for vigilance maintenance have shown inconsistent findings. However, [59] attributes the inconsistency due to the difference in experimental paradigms and stimuli that mostly included cognitive tasks requiring a high cognitive load; that is the *resource depletion theory*. Therefore, the authors of [59] conducted a simple d2-test that does not require significant mental workload to find brain areas where EEG activity is correlated with fluctuations in vigilance over prolonged time. They suggest that left prefrontal cortex is significantly correlated with vigilance variation.

The central and occipital regions show a slight increase in activity for low vigilance state. Their activity decreases again with challenge enhancement. A lower occipital activity at high vigilance state was also reported in [28]. The reverse trend for vigilance enhancements adds assurance to the occipital correlation to vigilance variations. The parietal shows a decrease with vigilance decrement. In [60], patients with parietal lesions as a group showed a significant impairment in processing speed, which could explain this decrease with vigilance decrement.

7.2 Conclusions

Vigilance decrement in tasks that resemble the *under-load hypothesis* can lead to serious penalties. Therefore exploring methods in continuous monitoring of vigilance can be of great importance. In this work, PSD and EEG source localization were used to investigate brain areas and aspects that are highly correlated to vigilance. It has been shown that the greatest indication of vigilance decrement lies in the prefrontal and frontal cortices. Additionally, electrodes with most sensitivity were found to be on the prefrontal cortex. Four EEG variables were used to construct an initial measurement model where 84.45% of prelabeled data were correctly identified. However, in order to improve the reliability of the vigilance measurement model, given the complexity of the neural circuits involved in maintaining vigilance, more brain dynamics can be used in conjunction to monitor vigilance fluctuations in

individuals undergoing monotonous tasks. Incorporating more variables and conducting longer experiments can lead to greater vigilance decrement and thus more accurate regression models for a more sensitive vigilance assessment.

7.3 Future Work

This report presented an insight on brain behavior dynamics in vigilance tasks using power spectral density and source localization analysis. The main purpose of this work is to construct a vigilance assessment model that can serve as a metric for quantifying vigilance levels in daily activities. In order to further improve the accuracy of the results, array processing algorithms that are robust to perturbations in leadfield matrix can be applied with the help of calibration techniques to improve localization and possibly reconstruct the signal emitted from the localized source. The nature of reconstructed signal from source localization can be studied with vigilance decrement. Further studies on ERPs behavior are to be applied to give insight about attention levels, such as magnitude and latency variations. The nature of localized sources coupled with power spectral density behavior of brainwaves can lead to an accurate vigilance assessment model. Integrating infrequent target signals in jobs with monotonous nature can be studied to facilitate monitoring vigilance levels. Additionally, for feasibility of implementation in daily activities, methods for analyzing single evoked response are to be considered.

References

[1] B. Oken, M. Salinsky, and S. Elsas, “Vigilance, alertness, or sustained attention: physiological basis and measurement,” *Clinical Neurophysiology*, vol. 117, no. 9, pp. 1885–1901, 2006.

[2] W. S. Helton and P. N. Russell, “Feature absence–presence and two theories of lapses of sustained attention,” *Psychological Research*, vol. 75, no. 5, pp. 384–392, 2010.

[3] W. S. Helton and P. N. Russell, “Working memory load and the vigilance decrement,” *Experimental Brain Research*, vol. 212, no. 3, pp. 429–437, Apr. 2011.

[4] N. Cao, I. Yetik, A. Nehorai, C. Muravchik, and J. Haueisen, “Estimating Parametric Line-Source Models With Electroencephalography,” *IEEE Transactions on Biomedical Engineering*, vol. 53, no. 11, pp. 2156–2165, 2006.

[5] R. Carter, *The Human Brain Book*, 2nd ed. New York: DK Publishing, 2014, pp 50-70.

[6] K. Cherry, "A Guide to the Anatomy of the Brain," *Verywell*, Aug. 30, 2016. [Online]. Available: https://www.verywell.com/the-anatomy-of-the-brain-2794895. [Accessed: Dec. 6, 2016].

[7] R. S. Swenson, "Cerebral cortical organization," in *Review of clinical and functional neuroscience*, Dartmouth Medical School, 2006 [On-line]. Available: http://www.dartmouth.edu/~rswenson/NeuroSci/index.html [Accessed: Dec. 5, 2016].

[8] "Transmission of Nerve Impulses," *cliffnotes.com*, [Online]. Available: https://www.cliffsnotes.com/study-guides/anatomy-and-physiology/nervous-tissue/transmission-of-nerve-impulses [Accessed: Dec. 6, 2016]

[9] “Propagation of the Action Potential,” *The University of Texas Medical School at Houston*. [Online]. Available: http://neuroscience.uth.tmc.edu/s1/chapter03.html. [Accessed: 26-Dec-2016].

[10] Raven, “Action potential propagation in an unmyelinated Axon,” *Biology Eighth Edition*. [Online]. Available: https://highered.mheducation.com/sites/9834092339/student_view0/chapter44/action_potential_propagation_in_an_unmyelinated_axon.html. [Accessed: 15-Dec-2016].

[11] “Brain Imaging Techniques.” *Boundless Psychology*, Aug. 08, 2016. https://www.boundless.com/psychology/textbooks/boundless-psychology-. [Accessed: 17-Jan-2017].

[12] “Positron Emission Tomography - Computed Tomography (PET/CT),” *Radiologyinfo.org*. [Online]. Available: http://www.radiologyinfo.org/en/info.cfm?pg=pet. [Accessed: 19-Dec-2016].

[13] “MRI Scans,” *MedlinePlus.com*. [Online]. Available: https://medlineplus.gov/mriscans.html. [Accessed: 16-Jan-2017].

[14] “Magnetic Resonance, Functional (fMRI)-Brain,” *Radiologyinfo.org*. [Online]. Available: http://www.radiologyinfo.org/en/pdf/fmribrain.pdf. [Accessed: 16-Jan-2017].

[15] "Functional Neuroimaging," *NYU Psychology*. [online]. Available: http://www.psych.nyu.edu/pylkkanen/Neural_Bases/07_slides/05_Methods.pdf . [Accessed: 16-Jan-2017].
[16] M. Teplan, "Fundamentals of EEG Measurement," *Measurement Science Review*, vol. 2, 2002.
[17] "What are Brainwaves," *Brainworksneurotherapy.com*. [Online]. Available: http://www.brainworksneurotherapy.com/what-are-brainwaves. [Accessed: 6-Jan-2017].
[18] "Brain Waves Frequencies," *Mental Health Daily*, Nov. 18, 2015. [Online]. Available: http://mentalhealthdaily.com/2014/04/15/5-types-of-brain-waves-frequencies-gamma-beta-alpha-theta-delta/. [Accessed: 06-Jan-2017].
[19] "Brainwaves," *DoctorHugo.org*. [Online]. Available: http://www.doctorhugo.org/brainwaves/brainwaves.html. [Accessed: 6-Jan-2017].
[20] A. P. F. Key, G. O. Dove, and M. J. Maguire, "Linking Brainwaves to the Brain: An ERP Primer," *Developmental Neuropsychology*, vol. 27, no. 2, pp. 183–215, 2005.
[21] "What is attention and where is it in the brain?," *Inside the brain*, Mar. 07, 2013. [Online]. Available: https://inside-the-brain.com/2013/03/07/what-is-attention-and-where-is-it-in-the-brain/. [Accessed: 04-Oct-2017].
[22] A. Trafton, "How the brain pays attention," *McGovern Institute for Brain Research at MIT*, Apr. 10, 2014. [Online]. Available: http://mcgovern.mit.edu/news/news/how-the-brain-pays-attention/. [Accessed: 06-Oct-2017].
[23] "Mapping brain circuits involved in attention," *National Institutes of Health*, Aug. 04, 2016. [Online]. Available: https://www.nih.gov/news-events/nih-research-matters/mapping-brain-circuits-involved-attention. [Accessed: 07-Oct-2017].
[24] J. Tanji and E. Hoshi, "Role of the Lateral Prefrontal Cortex in Executive Behavioral Control," *Physiological Reviews*, vol. 88, no.1, pp. 37-57, 2008. [Online]. Available: American Physiological Society, http://physrev.physiology.org. [Accessed: Oct. 15, 2017].
[25] I. P. Bodala, Y. Ke, H. Mir, N. V. Thakor, H. Al-Nashash, "Cognitive workload estimation due to vague visual stimuli using saccadic eye movements," *Annual International Conference Of The IEEE Engineering In Medicine And Biology Society. IEEE Engineering In Medicine And Biology Society. Annual Conference*, 2014, 2993-6. doi:10.1109/EMBC.2014.6944252
[26] Q. Ji, P. Lan, and C. Looney, "A probabilistic framework for modeling and real-time monitoring human fatigue," *IEEE Transactions on Systems, Man, and Cybernetics - Part A: Systems and Humans*, vol. 36, no. 5, pp. 862–875, 2006.
[27] I. P. Bodala, J. Li, N. V. Thakor, H. Al-Nashash, "EEG and Eye Tracking Demonstrate Vigilance Enhancement with Challenge Integration," *Frontiers In Human Neuroscience*, June, 2016. [Online]. Available: https://www.worldcat.org [Accessed: Dec. 6, 2016].
[28] J. Li, I. Prasad, J. Dauwels, N. V. Thakor, and H. Ai-Nashash, "Vigilance Differentiation from EEG Complexity Attributes," *Neural Information Processing Lecture Notes in Computer Science*, pp. 199–206, 2015.

[29] H. Ji, J. Li, L. Cao, and D. Wang, “A EEG-Based Brain Computer Interface System towards Applicable Vigilance Monitoring,” *Advances in Intelligent and Soft Computing Foundations of Intelligent Systems*, pp. 743–749, 2011.
[30] C. Lei et al., "EEG-based vigilance analysis by using fisher score and PCA algorithm," in *2010 IEEE International Conference on Progress in Informatics and Computing*, 2010, pp. 175-179.
[31] F. Sauvet, C. Bougard, M. Coroenne, L. Lely, P. V. Beers, M. Elbaz, M. Guillard, D. Leger, M. Chennaoui, " In-Flight Automatic Detection of Vigilance States Using a Single EEG Channel," *IEEE Transactions on Biomedical Engineering*, 2014, vol. 61, no. 12, p. 2840.
[32] M. Hämäläinen, R. Hari, R. J. Ilmoniemi, J. Knuutila, and O. V. Lounasmaa, "Magnetoencephalography—theory, instrumentation, and applications to noninvasive studies of the working human brain," *Reviews of Modern Physics*, vol. 65, no. 2, pp. 413-497, 1993.
[33] J. Mosher, P. Lewis, and R. Leahy, “Multiple dipole modeling and localization from spatio-temporal MEG data,” *IEEE Transactions on Biomedical Engineering*, vol. 39, no. 6, pp. 541–557, 1992.
[34] F. Vatta, F. Meneghini, F. Esposito, S. Mininel, and F. D. Salle, “Realistic and Spherical Head Modeling for EEG Forward Problem Solution: A Comparative Cortex-Based Analysis,” *Computational Intelligence and Neuroscience*, vol. 2010, pp. 1–11, 2010.
[35] C.M. Michel, M. M. Murray, G. Lantz, S. Gonzalez, L. Spinelli, and R. Grave de Peralta, "EEG Source Imaging," *Clinical Neurophysiology: Official Journal of the International Federation of Clinical Neurophysiology*, vol. 115, no. 10, pp. 2195-222, 2004.
[36] Z. A. Acar, S. Makeig, and G. Worrell, “Head modeling and cortical source localization in epilepsy,” *2008 30th Annual International Conference of the IEEE Engineering in Medicine and Biology Society*, 2008.
[37] S. Baillet, J. J. Riera, G. Marin, J. F. Mangin, J. Aubert, and L. Garnero, “Evaluation of inverse methods and head models for EEG source localization using a human skull phantom,” *Physics in Medicine and Biology*, vol. 46, no. 1, pp. 77–96, 2000.
[38] S. Baillet, J. Mosher, and R. Leahy, “Electromagnetic brain mapping,” *IEEE Signal Processing Magazine*, vol. 18, no. 6, pp. 14–30, 2001.
[39] R. Grech, T. Cassar, J. Muscat, K. P. Camilleri, S. G. Fabri, M. Zervakis, P. Xanthopoulos, V. Sakkalis, and B. Vanrumste, “Review on solving the inverse problem in EEG source analysis,” *Journal of NeuroEngineering and Rehabilitation*, vol. 5, no. 1, p. 25, 2008.
[40] J. Mosher and R. Leahy, “Recursive MUSIC: A framework for EEG and MEG source localization,” *IEEE Transactions on Biomedical Engineering*, vol. 45, no. 11, pp. 1342–1354, 1998.
[41] B. V. Veen, W. V. Drongelen, M. Yuchtman, and A. Suzuki, “Localization of brain electrical activity via linearly constrained minimum variance spatial filtering,” *IEEE Transactions on Biomedical Engineering*, vol. 44, no. 9, pp. 867–880, 1997.
[42] J. Mosher and R. Leahy, “Source localization using recursively applied and projected (RAP) MUSIC,” *IEEE Transactions on Signal Processing*, vol. 47, no. 2, pp. 332–340, 1999.

[43] M. S. Hämäläinen and R. J. Ilmoniemi, “Interpreting magnetic fields of the brain: minimum norm estimates,” *Medical & Biological Engineering & Computing*, vol. 32, no. 1, pp. 35–42, 1994.
[44] M. A. Jatoi, N. Kamel, A. S. Malik, I. Faye, and T. Begum, "A survey of methods used for source localization using EEG signals," *Biomedical Signal Processing and Control*, vol. 11, pp. 42-52, 5, 2014.
[45] K. Kaiboriboon, H. O. Luders, M. Hamaneh, J. Turnbull, and S. D. Lhatoo, "EEG source imaging in epilepsy-practicalities and pitfalls," *Nature Reviews Neurology*, vol. 8, no. 9, pp. 498-507, 2012.
[46] M. A. Jatoi, N. Kamel, A. S. Malik, and I. Faye, “EEG based brain source localization comparison of sLORETA and eLORETA,” *Australasian Physical & Engineering Sciences in Medicine*, vol. 37, no. 4, pp. 713–721, 2014.
[47] I. F. Gorodnitsky, J. S. George, and B. D. Rao, “Neuromagnetic source imaging with FOCUSS: a recursive weighted minimum norm algorithm,” *Electroencephalography and Clinical Neurophysiology*, vol. 95, no. 4, pp. 231–251, 1995.
[48] M. Popescu, S. D. Blunt, and T. Chan, "Magnetoencephalography source localization using the source affine image reconstruction (SAFFIRE) algorithm," (in eng), *IEEE Trans Biomed Eng*, vol. 57, no. 7, pp. 1652-62, Jul 2010.
[49] N. N. Boutros and I. Ebrary, “Standard electroencephalography in clinical psychiatry: a practical handbook,”. Hoboken, NJ; Chichester, West Sussex; Wiley-Blackwell, 2011.
[50] J. G. Temple, J. S. Warm, W. N. Dember, K. S. Jones, C. M. LaGrange, and G. Matthews, "The effects of signal Salience and caffeine on performance, workload, and stress in an abbreviated vigilance task," *Human Factors: The Journal of the Human Factors and Ergonomics Society*, vol. 42, no. 2, pp. 183–194, Jun. 2000.
[51] “Asa User Manual”, *Ant Neuro Inspiring Technology*. ver. 4.10.1, July, 2016.
[52] K Yu, I Prasad, H Mir, N Thakor, Hasan Al-Nashash, “Cognitive Workload Modulation Through Degraded Visual Stimuli: a Single-Trial EEG Study” *Journal of Neural Engineering*, vol 12, no. 9, June 2015.
[53] J. Polich, “Updating P300: An Integrative Theory of P3a and P3b,” *Clinical neurophysiology: official journal of the International Federation of Clinical Neurophysiology*, vol. 118, no. 10, pp. 2128-2148, 2007. doi:10.1016/j.clinph.2007.04.019.
[54] D. Timmers, “Treating Attention Deficits and Impulse Control,” *Clinical Neurotherapy*, pp. 139–169, 2014.
[55] L. Greensfelder, “Brain Wave Patterns Can Predict Blunders, New Study Finds,” *UCDavis.edu*, Jan. 23, 2016. [Online]. Available: https://www.ucdavis.edu/news/brain-wave-patterns-can-predict-blunders-new-study-finds. [Accessed: 05-Nov-2017].
[56] “Vigilance and the Brain,” *Tuck Sleep*. [Online]. Available: https://www.tuck.com/vigilance/. [Accessed: 05-Nov-2017].
[57] R. Parasuraman, and G. Caggiano, “Neural and genetic assays of mental workload”. In D. McBride and D. Schmorrow Ed. *Quantifying Human Information Processing*, pp 123–155, 2005. Lanham, MD: Rowman & Littlefield.

[58] T.H. Shaw, J. S. Warm, V. Finomore, L. Tripp, G. Matthews, E. Weiler, & R. Parasuraman,"Effects of sensory modality on cerebral blood flow velocity during vigilance," *Neuroscience Letters* 461, pp. 207-211, 2009.
[59] J. H. Kim, D.W. Kim, and C.H. Im, "Brain Areas Responsible for Vigilance: An EEG Source Imaging Study," *Brain Topography,* Jan-2017. doi: 10.1007/s10548-016-0540-0.
[60] P. V. Peers, C.J.H. Ludwig, C. Rorden, R. Cusack, C. Bonfiglioli, C. Bundesen, J. Driver, N. Antoun and J. Duncan, "Attentional functions of parietal and frontal cortex," *Cerebral Cortex,* vol. 15, pp. 1469- 1484, 2005.

Vita

Salma was born in 1993, in Cairo, Egypt. She received her primary and secondary education in Cairo, Egypt. She finished her high school studies in Dubai UAE. She received her B.Sc. degree in Electrical Engineering from the American University in Sharjah in 2015.

In September 2015, she joined the Electrical Engineering master's program in the American University of Sharjah as a graduate teaching assistant. Her research interests are in signal processing, machine learning, and applied estimation.